

## Supporting information

### Biomimetic hairy affective-touch sensory AI interface

Jianlong Hong <sup>1,2,3,#</sup>, Yukun Xiao <sup>1,#</sup>, Yuqi Chen <sup>1</sup>, Shengshun Duan <sup>1</sup>, Shengxin Xiang <sup>1</sup>, Xiao Wei <sup>1</sup>, Huiyun Zhang <sup>1</sup>, Lei Liu <sup>1</sup>, Jun Xia <sup>1</sup>, Wei Lei <sup>1</sup>, Qiongfeng Shi <sup>1\*</sup>, Chengkuo Lee <sup>2,3\*</sup>,  
Jun Wu <sup>1\*</sup>

<sup>1</sup> Interdisciplinary Research Center, School of Electronic Science and Engineering, Southeast University, Nanjing 211189, China

<sup>2</sup> Department of Electrical and Computer Engineering, National University of Singapore, Singapore, Singapore

<sup>3</sup> Center for Intelligent Sensors and MEMS (CISM), National University of Singapore, Singapore, Singapore

# These authors contributed equally.

Email: [qiongfeng@seu.edu.cn](mailto:qiongfeng@seu.edu.cn) (Q. Shi); [elelc@nus.edu.sg](mailto:elelc@nus.edu.sg) (C. Lee) [wujunseu@seu.edu.cn](mailto:wujunseu@seu.edu.cn) (J. Wu)

## Supplementary Note 1 | Theoretical modeling of the triboelectric pulse generation process in the BioAI<sup>2</sup>.

We have developed a theoretical model to provide a quantitative description of the spike generation mechanism.

For analytical simplicity, given the complexity of the contact interface involving multiple hairs, our primary analysis centers on a simplified model of a single hair interacting with a finger. The contact-electrification process for a single hair in the BioAI<sup>2</sup> is illustrated in Supplementary Fig. 2a. The system involves multiple capacitors between the finger and the electrode, primarily comprising the contact capacitance at the touch point ( $C_{Con}$ ), the non-contact air gap capacitance ( $C_{Air}$ ), and the dielectric capacitance of the hair ( $C_D$ ).

The equivalent electrical model is simplified as shown in Supplementary Fig. 2b. Dielectric 1 represents the skin, and dielectric 2 represents the hair's media layer, with surface charge densities of  $-\sigma$  and  $+\sigma$  respectively, due to contact electrification. The sensing electrode carries an induced charge  $Q$ , while the ground electrode has a transferred charge  $-Q$ .

Under open-circuit (OC) conditions ( $Q = 0$ ), an equivalent circuit model was established (Supplementary Fig. 2c). The key nodes are: Node 1 (dielectric 1 surface), Node 2 (dielectric 2 surface), Node 3 (sensing electrode), and Node 4 (ground electrode). Capacitances exist between each node pair due to electric field lines. The total capacitance between Node 3 and 4,  $C_0$ , is given by:

$$C_0 = C_S + \frac{C_H C_D C_E}{C_H C_D + C_H C_E + C_D C_E} \quad (1)$$

Where  $C_H = C_{Air} + C_{Con}$ .

Based on charge conservation at each node and the defined potential relationships, we derived the following equation (the positive direction is shown in Supplementary Fig. 2c):

$$V_E = V_H + V_D + V_S \quad (2)$$

$$C_E V_E + C_H V_H = \sigma S \quad (3)$$

$$C_D V_D - C_H V_H = -\sigma S \quad (4)$$

$$C_S V_S = C_D V_D \quad (5)$$

$$-C_E V_E - C_S V_S = 0 \quad (6)$$

Combine the Equation (2-6), we can derive the open-circuit voltage:

$$V_S = V_{OC} = \frac{C_E C_D \sigma S}{C_H C_D C_E + C_H C_D C_S + C_H C_E C_S + C_D C_E C_S} \quad (7)$$

Following the theoretical framework for TENGs<sup>4</sup>, the general voltage-charge relationship is:

$$V = -\frac{1}{C} \times Q + V_{OC} \quad (8)$$

Under short-circuit (SC) conditions ( $V=0$ ), the short-circuit transferred charge ( $Q_{SC}$ ) is:

$$0 = -\frac{1}{C} \times Q_{SC} + V_{OC} \quad (9)$$

$$Q_{SC} = V_{OC} C \quad (10)$$

Substituting equations (1) and (7) into (10) yields the core model for  $Q_{SC}$ :

$$Q_{SC} = V_{OC}C_0 = \frac{\sigma S}{C_H \times \left(\frac{1}{C_D} + \frac{1}{C_E}\right) + 1} \quad (11)$$

Since  $C_H = C_{Air} + C_{Con}$ , this becomes:

$$Q_{SC} = V_{OC}C_0 = \frac{\sigma S}{(C_{Air} + C_{Con}) \times \left(\frac{1}{C_D} + \frac{1}{C_E}\right) + 1} \quad (12)$$

This model explicitly incorporates the surface charge density ( $\sigma$ ) resulting from contact electrification, addressing the surface potential dynamics mentioned by the reviewer. The dynamics are governed by the time-dependent changes in the capacitances  $C_{Air}$  and  $C_{Con}$  during the finger's approach and contact with the hair. There are two phases during this process.

**1. Non-contact phase ( $C_{Con} = 0$ ):** The air gap capacitance is:

$$C_{Air} = \frac{\varepsilon_0 \varepsilon_{r0} S}{d(t)} \quad (13)$$

where  $\varepsilon_0$  is the dielectric constant of vacuum,  $\varepsilon_{r0}$  is the relative dielectric constant of air, and  $d$  is the distance between the finger and the hair.

Substituting Equation (13) into Equation (12), we have:

$$Q_{SC} = \frac{\sigma S}{\frac{\varepsilon_0 \varepsilon_{r0} S}{d(t)} \times \left(\frac{1}{C_D} + \frac{1}{C_E}\right) + 1} \quad (14)$$

According to Equation (13) and (14), as the finger approaches ( $d(t)$  decreases),  $C_{Air}$  increases, leading to a specific dynamic change in  $Q_{SC}$ , which we calculated and plotted (see simulation in Supplementary Fig. 3).

**2. Contact phase ( $C_{Air} \ll C_{Con}$ ):** Upon contact, the  $C_{Air}$  is much smaller than the contact capacitance  $C_{Con}$ . Therefore, the  $C_{Air}$  can be neglected. The  $C_{Con}$  can be calculated as:

$$C_{Con} = \frac{\varepsilon_0 \varepsilon_r S_1(t)}{d_1} \quad (15)$$

where the  $\varepsilon_r$  is the composite relative permittivity of the skin and dielectric layer 1, the contact area  $S_l$  is a function of time, and  $d_l$  is the thickness of the contact capacitance, which can be regarded as a fixed value.

Substituting equation (15) into equation (12), we have:

$$Q_{SC} = \frac{\sigma S}{\frac{\varepsilon_0 \varepsilon_r S_1(t)}{d_1} \times \left(\frac{1}{C_D} + \frac{1}{C_E}\right) + 1} \quad (16)$$

$C_{Con}$  is a function of the contact area  $S_l(t)$ , which changes over time during the sliding motion. This variation directly drives the major change in  $Q_{SC}$ .

On the basis of the discussion and the parameter as shown in Supplementary Table 2, we can obtain the dynamic variation of the transfer charge (Supplementary Fig. 3).

The corresponding short-circuit current ( $I_{SC}$ ) can be calculated as:

$$I_{SC} = \frac{dQ_{SC}}{dt} \quad (17)$$

Therefore, the dynamic variation of  $I_{SC}$  is shown in Supplementary Fig. 4.

The results clearly demonstrate that the current signal exhibits a distinct neural spike-like behavior, stemming directly from the dynamics of the capacitive coupling modeled above.

The voltage output behavior under limited load ( $1\text{ M}\Omega$ ) is similar to the output behavior of  $I_{SC}$ . And thus, the neuromimetic pulse output is demonstrated.

## Supplementary Note 2 | Elaboration on the analogy of BioAI<sup>2</sup> to C-LTMRs.

The analogy of BioAI<sup>2</sup> to C-LTMRs is based on three key aspects: structural analogy, neuronal encoding principles, and functional response characteristics.

### 1. Structural analogy: hairy skin as a shared sensory platform

Both the BioAI<sup>2</sup> interface and biological C-LTMRs operate within the context of hairy skin. This is a fundamental architectural similarity. In mammals, C-LTMRs specifically innervate hairy skin, where hair follicles act as intrinsic mechanical levers that amplify gentle tactile stimuli<sup>7,8</sup> (Supplementary Fig. 4a). Similarly, the BioAI<sup>2</sup>'s design features an array of artificial hairs (Supplementary Fig. 4b). These hairs serve as the primary mechanical interface that transduces mechano-stimulation into electrical signals, mimicking the role of hair follicles in directing mechanical forces onto the C-LTMR endings in biological systems. This establishes a foundational structural biomimesis where the external stimulus pathway is analogous.

### 2. Neuro-mimetic encoding principles: a coupled biophysical model

To move beyond a mere visual comparison, we have developed a coupled biophysical model that links the device's physics to neural encoding principles. As detailed in the previous question, the triboelectric effect governs the charge generation ( $V, Q$ ) in response to mechanical contact and separation (simulating touch). This electrical signal serves as the input to a simplified leaky integrate-and-fire (LIF) neuron model. The LIF model is a well-established computational framework in neuroscience for simulating the membrane potential dynamics of neurons (Supplementary Fig. 4c,d). In our model, the triboelectrically induced current charges a capacitor representing the neuronal membrane (Supplementary Fig. 4e). Once the hand contacts and leaves the hair, the capacitor will be charged and released, and a spike is generated. The hair acts as a mechanical switch here. This coupling directly simulates the process of mechano-transduction and encoding in a primary afferent: mechanical stimulus  $\rightarrow$  receptor potential  $\rightarrow$  action potential generation. This approach provides a principled model, rather than a mere analogy, for the spike generation mechanism that underlies the neuromimetic behavior.

### 3. Functional biomimesis: quantifying the “inverted U-shaped” response

We have further strengthened the analogy by quantitatively comparing the stimulus-response functions. A hallmark of C-LTMR physiology is their inverted U-shaped response to stroking speed, with peak sensitivity in the slow range (approximately 1-10 cm/s in humans, correlating with pleasant touch<sup>11</sup>). Our experimental results and model simulations demonstrate that BioAI<sup>2</sup> exhibits a strikingly similar inverted U-shaped frequency-stroking speed response. Supplementary Table 3 provides a direct, quantitative comparison of key response properties between BioAI<sup>2</sup> and biological C-LTMRs, substantiating the functional equivalence beyond visual similarity.

### Supplementary Note 3 | Calculation of the coordinates of the touch point.

As shown in Fig. 2j, the equivalent circuit of the BioAI<sup>2</sup> reveals that the voltage on electrode 1 and the equivalent resistance of the circuit can be calculated as:

$$V_1 = I_1 R_{ex} \quad (18)$$

$$R_{sum} = \frac{1}{\frac{1}{R_{ex} + R_1} + \frac{1}{R_{ex} + R_2} + \frac{1}{R_{ex} + R_3} + \frac{1}{R_{ex} + R_4}} \quad (19)$$

According to Ohm's Law, the voltage of the contact point could be calculated as:

$$V = I_1(R_{ex} + R_1) = R_{sum} \cdot I \quad (20)$$

Thus,

$$V_1 = \frac{1}{R_{sum}(R_{ex} + R_1)} \cdot I R_{ex} \quad (21)$$

Similarly, the voltage on electrodes 1, 2, 3 can be obtained as well. Therefore, the widely used coordinates calculation formulas can be calculated as:

$$x = \frac{V_1 + V_2}{V_1 + V_2 + V_3 + V_4} = \frac{\frac{1}{R_{ex} + R_1} + \frac{1}{R_{ex} + R_2}}{\frac{1}{R_{ex} + R_1} + \frac{1}{R_{ex} + R_2} + \frac{1}{R_{ex} + R_3} + \frac{1}{R_{ex} + R_4}} \quad (22)$$

$$y = \frac{V_1 + V_4}{V_1 + V_2 + V_3 + V_4} = \frac{\frac{1}{R_{ex} + R_1} + \frac{1}{R_{ex} + R_4}}{\frac{1}{R_{ex} + R_1} + \frac{1}{R_{ex} + R_2} + \frac{1}{R_{ex} + R_3} + \frac{1}{R_{ex} + R_4}} \quad (23)$$

Here, due to the resistance of the conductive layer ( $> 100 \text{ M}\Omega$ ) is much larger than that of the input resistance of the voltage detector ( $1 \text{ M}\Omega$ ),  $R_{ex}$  can be ignored when the touch point is not close to the electrode. Thus, we have:

$$x = \frac{V_1 + V_2}{V_1 + V_2 + V_3 + V_4} \approx \frac{\frac{1}{R_1} + \frac{1}{R_2}}{\frac{1}{R_1} + \frac{1}{R_2} + \frac{1}{R_3} + \frac{1}{R_4}} \quad (24)$$

$$y = \frac{V_1 + V_4}{V_1 + V_2 + V_3 + V_4} \approx \frac{\frac{1}{R_1} + \frac{1}{R_4}}{\frac{1}{R_1} + \frac{1}{R_2} + \frac{1}{R_3} + \frac{1}{R_4}} \quad (25)$$

#### **Supplementary Note 4 | Explanation of isoline plots of ratios $x$ and $y$**

Figure 3(g) presents isoline plots of two ratios,  $x$  and  $y$ , which are calculated using Equation (5) and (6).

The plotting procedure was as follows:

Firstly, we calculated the values of ratio  $x$  for every point across the entire X-Y plane based on Equation (9).

Secondly, using scientific plotting software (MATLAB), we generated the isolines for ratio  $x$ . Each isoline (represented by red curves in Fig. 10a) connects all points sharing the same value of  $x$ . The color intensity of the lines corresponds to the magnitude of  $x$ . Similarly, we calculated and plotted the isolines for ratio  $y$  (represented by blue curves in Fig. 10(b)).

Finally, Fig. 3(g) was created by superimposing the isoline plots of  $x$  and  $y$ .

### **Supplementary Note 5 | Elaboration on stroking trajectory positioning.**

Figure 3(k) showcases the reconstructed stroking trajectories of two fingers, demonstrating the practical application of our method. The reconstructing procedure was as follows:

Firstly, as two fingers stroke across the BioAI<sup>2</sup> interface, they generate a series of dense voltage pulse peaks on the four electrodes (Supplementary Fig. 19(i)). Secondly, the raw data is acquired and then processed with a bandpass filter (50 Hz ~ 600 Hz) to remove low-frequency signal components and baseline drift (Supplementary Fig. 19 (ii)). Thirdly, valid pulse peaks that meet specific criteria are identified from the filtered signal (Supplementary Fig. 19 (iii)). Fourthly, for each pair of valid peaks (corresponding to a specific time point), the touch coordinate is calculated using the isoline intersection method described for Fig. 3(h) (Supplementary Fig. 19 (iv)). Finally, all the calculated coordinate points for each finger are plotted sequentially. The color of the points transitions from red (early in time) to blue (later in time), forming the continuous trajectories shown in Fig. 3(k).

## **Supplementary Note 6 | Elaboration on precise mapping process between action features and emotion labels.**

### **Theoretical Basis:**

A growing body of literature has established strong correlations between tactile action features and emotional experiences. From a neurophysiological perspective, affective touch is specifically mediated by C-low-threshold mechanoreceptors (C-LTMRs). In particular, MRGPRB4 + neurons—which are selectively expressed in C-LTMRs—have been shown to respond to massage-like stroking but not to noxious mechanical stimuli. Moreover, optogenetic activation of these neurons induced conditioned place preference in mice, suggesting their role in positive affective processing<sup>16</sup>. This provides a neurobiological basis for linking specific tactile actions (e.g., gentle stroking) to positive emotional states.

Furthermore, multiple psychophysical studies support the relationship between tactile kinematics and emotional dimensions (valence and arousal). For example, Teyssier et al. demonstrated that variations in touch velocity (3.8, 16 cm/s) and force (0.3, 1.2 N) significantly modulate emotional valence and arousal<sup>18</sup>. Similarly, Hertenstein et al. and McIntyre et al. showed that humans can accurately decode distinct emotions—including anger, fear, love, and gratitude—via touch alone, confirming that tactile actions carry emotionally relevant information<sup>19,20</sup>.

### **Methodological Details:**

Our artificial hair sensor was specifically designed to capture tactile features associated with C-LTMR responses. As shown in Fig. 2g–h, the sensor’s spiking frequency varies with stroking speed in a manner analogous to biological C-LTMRs. Additionally, its force sensitivity (Fig. 3d) covers the typical range of human affective touch (e.g., gentle stroking or pressing). These characteristics ensure that the sensor reliably encodes key kinematic parameters (speed, force, location) relevant to emotional communication.

To establish a robust mapping from sensor outputs to emotion labels, we conducted controlled subjective experiments involving 13 participants. Each tactile gesture was accompanied by real-time emotional ratings using the Self-Assessment Manikin (SAM)<sup>21</sup>—a widely adopted instrument for assessing valence and arousal. This design ensures that the recorded sensor data correspond to ground-truth emotional labels. A neural network was then trained on this dataset to learn the complex, non-linear relationship between tactile features and emotional dimensions.

### **Logical Reasoning:**

The mapping process is built on the following logic:

1. Neurophysiological and behavioral evidence confirms that specific tactile features (e.g., low force, moderate velocity) elicit consistent emotional responses.
2. Our sensor replicates the encoding properties of biological affective touch receptors.
3. By collecting synchronized tactile-action and emotion-label data under controlled conditions, we align sensor outputs with psychologically validated emotional states.

4. The neural network serves as a data-driven function approximator that generalizes the feature–emotion relationship beyond the training set.

## **Supplementary Note 7 | Comparative analysis between ChatGPT and other transformers.**

While sentiment analysis capabilities of Transformers and GPT were not the primary focus of our research direction, empirical evidence from existing literature supports their strong performance in sentiment understanding. Specifically, BERT and other Transformer-based models, when fine-tuned on dedicated datasets, can achieve high accuracy in specific task scenarios. In contrast, models like GPT offer distinct advantages in zero-shot or few-shot sentiment analysis without requiring extensive task-specific fine-tuning.

For instance, David et al. conducted a comparative analysis using a database of 30,000 COVID-19-related tweets to evaluate the sentiment analysis and emotion classification capabilities of GPT-3.5 and IBM Watson<sup>22</sup>. Their findings indicate that GPT-3.5's contextual prompting approach enables it to better grasp nuanced elements such as sarcasm, despite not being explicitly trained for sentiment analysis.

Further supporting this, Jan et al. evaluated the performance of high-performance transfer learning models like RoBERTa against state-of-the-art LLMs—including GPT-3.5, GPT-4, and Llama 2—in zero-shot, three-class sentiment classification tasks on a dataset of 792 text documents from Amazon, Flipkart, and Twitter<sup>23</sup>. Their results showed that GPT-4 achieved the highest classification accuracy in three out of four datasets, with an average performance at least 4.9 percentage points higher than other LLMs and RoBERTa. While RoBERTa, fine-tuned on a corpus containing over 5,000 social media posts, excelled in one specific Twitter dataset, highlighting the advantage of model specialization, the overall strong zero-shot performance of LLMs like GPT-4 is evident. The experimental results underscore the outstanding zero-shot performance of LLMs in sentiment analysis. However, they also emphasize that specialized, fine-tuned transfer learning models like RoBERTa can outperform LLMs in certain scenarios.

Additionally, without additional training, Jeana et al. compared a lexicon-based model (VADER), a deep learning Transformer-based model (Twitter-roBERTa-base), and a GPT-based model (GPT-4o mini) for sentiment analysis on an energy transition-related tweet corpus containing 1,000 manually annotated English tweets<sup>24</sup>. The result demonstrated that the GPT-based model outperformed the other two approaches, further underscoring the high performance of GPT in zero-shot settings.

In summary, while specialized, fine-tuned Transformer models like BERT excel in specific understanding tasks, GPT's robust zero-shot and few-shot learning capabilities make it particularly suitable for the application scenario proposed in our study, where extensive task-specific training is not feasible.

## Supplementary Note 8 | Experimental validation of the contribution of contextual information and tactile emotion cues to ChatGPT's.

To analyze the contribution of contextual information and tactile emotion cues to ChatGPT's reasoning, we conducted a comparative experiment. The scenario was set as the owner returning home from work. The contextual information provided was: *"Imagine a scenario where there is a man who is lively, cheerful and loves life. He has a dog. One evening, the man comes home from work."* The tactile emotion cues given was: *"The man strokes the dog and his mood is negative."* Under three conditions—contextual information only, tactile emotion cues only, and both contextual information and tactile emotion cues—we asked ChatGPT to quantify the likelihood of the owner being in different emotional states. The corresponding results are as follows:

### Experiment 1: Contextual information only

[CONTEXTUAL INFORMATION] Imagine a scenario where there is **a man who is lively, cheerful and loves life**. He has a dog. One evening, the man **comes home from work**.

[AFFECTIVE TACTILE INPUT] **None**.

[USER QUERY 1] I need you to play as the dog to further analyze the owner's mood. Please quantify the possibilities of the owner under different emotions.

[CHATGPT OUTPUT]

➤ Positive Mood – Happy / Relieved / Excited (Probability: **55%**)

Interpretation: Work went well, maybe got praised or finished something important. Ready to relax but energized by being home.

➤ Neutral Mood – Tired / Content / Calm (Probability: **30%**)

Interpretation: A regular day. Nothing special happened. Physically tired but emotionally neutral. Looking forward to rest and maybe some quiet time together.

➤ Negative Mood – Stressed / Sad / Frustrated (Probability: **15%**)

Interpretation: Something didn't go right today. Could be work stress, personal issue, or just general fatigue. Needs space or comfort.

### Experiment 2: Tactile emotion cues only

[CONTEXTUAL INFORMATION] **None**.

[AFFECTIVE TACTILE INPUT] The man **strokes** the dog and his mood is **negative**.

[USER QUERY 1] I need you to play as the dog to further analyze the owner's mood. Please quantify the possibilities of the owner under different emotions

[CHATGPT OUTPUT]

➤ Sadness (Probability: **40%**)

Interpretation: The man may have had a loss, bad news, or is just having a hard day. My presence seems comforting, but he's not perking up.

➤ Stress/Anxiety (Probability: **35%**)

Interpretation: Something is on his mind—work pressure, family issues, or general worry. He seeks calm through me, but it's not fully working.

➤ Guilt or Self-Blame (Probability: **10%**)

Interpretation: Maybe he feels like he's not being a good owner right now, or something happened that he thinks he could've prevented.

➤ Anger (Probability: **10%**)

Interpretation: If he were truly angry, I'd feel it in his grip. It's possible he's mad at someone else or about a situation, but he's redirecting that emotion by seeking comfort in routine.

➤ Depression (Probability: 5%)

Interpretation: This is rarer, but if it's been going on for days, I'd be concerned. He may need more than my company to recover.

### Experiment 3: Both contextual information and tactile emotion cues

[CONTEXTUAL INFORMATION] Imagine a scenario where there is a **man who is lively, cheerful and loves life**. He has a dog. One evening, the man **comes home from work**.

[AFFECTIVE TACTILE INPUT] The man **strokes** the dog and his mood is **negative**.

[USER QUERY 1] I need you to play as the dog to further analyze the owner's mood. Please quantify the possibilities of the owner under different emotions

[CHATGPT OUTPUT]

➤ Tired + Frustrated (Probability: 45%)

Interpretation: Work probably didn't go great. Deadlines, meetings, maybe someone took credit for your idea. You're holding it together, but you're worn out and a bit frustrated.

➤ Worried or Anxious About Something (Probability: 25%)

Interpretation: Something is on his mind—work pressure, family issues, or general worry. He seeks calm through me, but it's not fully working.

➤ Disappointed or Discouraged (Probability: 15%)

Interpretation: Maybe someone criticized you unfairly. Maybe things didn't go your way despite effort. Whatever it was, it hit you harder than you show.

➤ Irritated / Annoyed (Probability: 10%)

Interpretation: You're annoyed—probably not at me (thank goodness)—but at something or someone who got under your skin. Could be traffic. Could be Karen from accounting again.

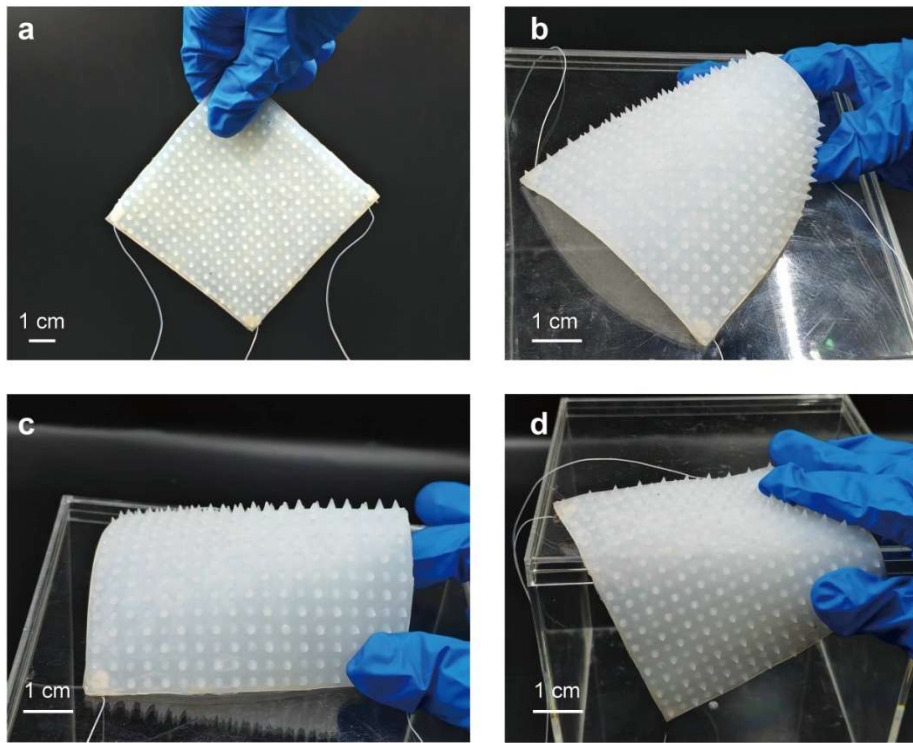
➤ Feeling Blue / Emotionally Drained (Probability: 5%)

Interpretation: Today wasn't just bad—it drained you emotionally. Maybe you smiled all day for others, but now you're alone, and the mask is off.

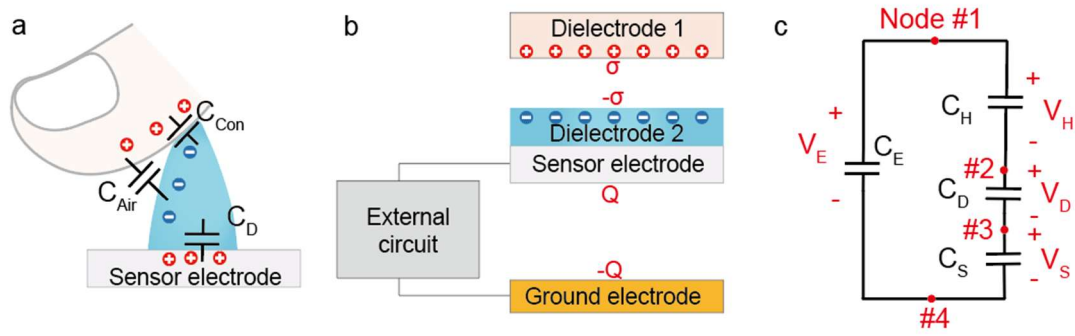
From the results, in the contextual information-only condition, ChatGPT could not determine whether the person's emotion was positive, neutral, or negative, though it still showed a bias toward positive emotion (probability up to 55%) based on the owner's generally cheerful personality. In the tactile emotion cues-only condition, ChatGPT's judgment clearly leaned toward negative emotion, yet this negative emotion could be classified into many possible categories (e.g., Sadness 40%, Stress/Anxiety 35%). Without scenario information, ChatGPT could not specify which category was most plausible. In the combined condition (both contextual information and tactile emotion cues), ChatGPT's judgment still exhibited a clear negative emotional tendency, but the classification became more concentrated (Tired + Frustrated 45%, other emotions  $\leq 25\%$ ). This demonstrates that having both contextual information and tactile emotion cues helps ChatGPT more confidently determine the owner's precise emotional category.

The results clearly demonstrate that:

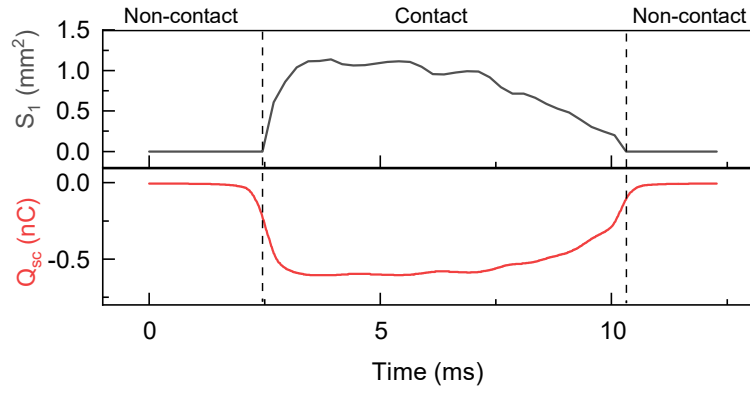
- Tactile emotion cues primarily determine the basic emotional valence (positive, neutral, negative). In the fused condition, the output correctly aligns with the negative label provided by the CNN.
- Contextual information is crucial for refining the coarse emotion into a specific, nuanced category. It helps disambiguate the reason behind the tactile cue by integrating scenario knowledge.
- The fusion of both components yields a more confident, precise, and contextually appropriate emotional interpretation than either modality alone. Thus, ChatGPT incorporates contextual information (scenario, user/dog profiles, relationship) to refine the coarse emotional labels from the CNN. This enables nuanced interpretation through advanced reasoning, aligning with higher-order cognitive processes.



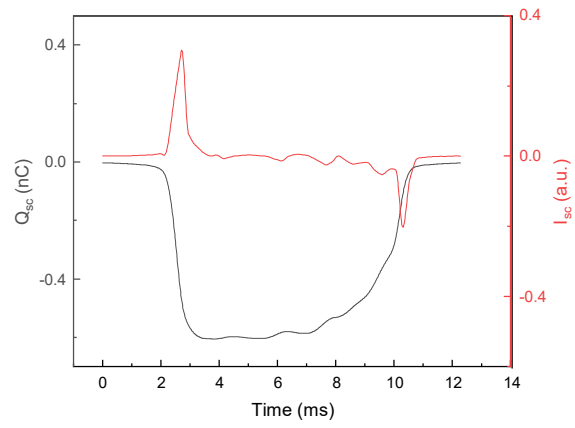
**Supplementary Fig. 1 | Optical images of the BioAI<sup>2</sup>.** **a** Appearance of the BioAI<sup>2</sup>. **b-d** Flexibility of the BioAI<sup>2</sup>.



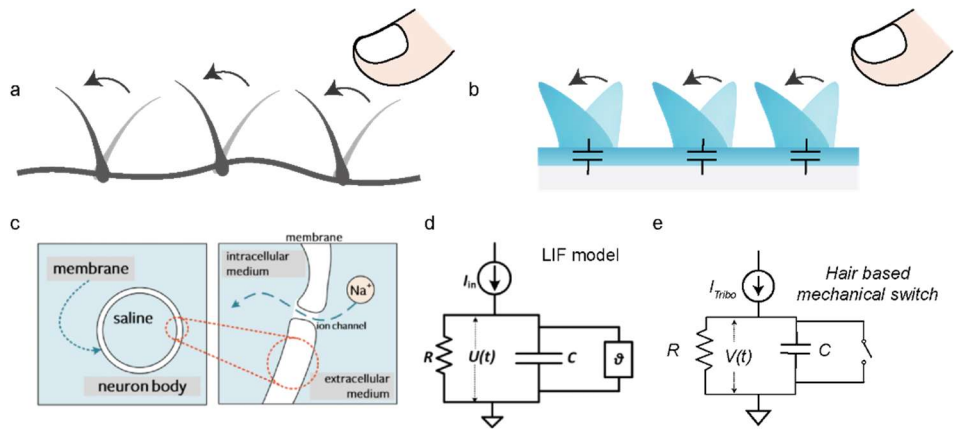
**Supplementary Fig. 2 | Theoretical model of BioAI<sup>2</sup>.**



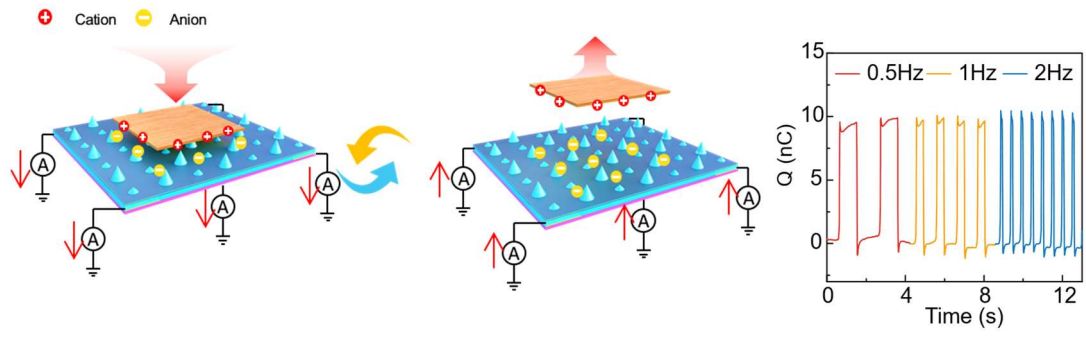
**Supplementary Fig. 3 | Simulation result of contact area (black) and the calculated short-circuit transfer charge (red).**



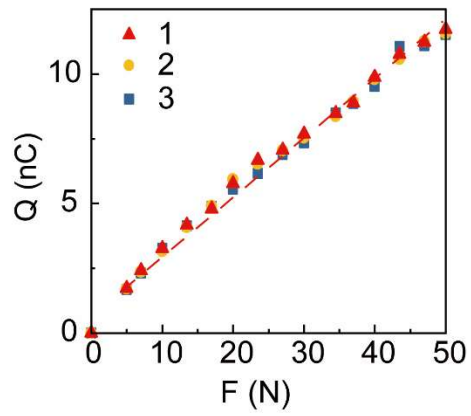
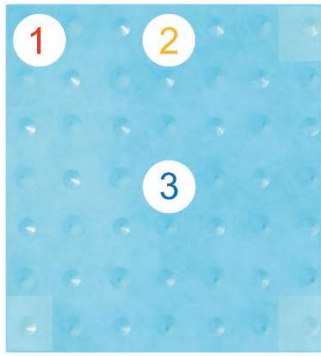
**Supplementary Fig. 4 | Simulated  $I_{SC}$  (red) from  $Q_{SC}$  (black).**



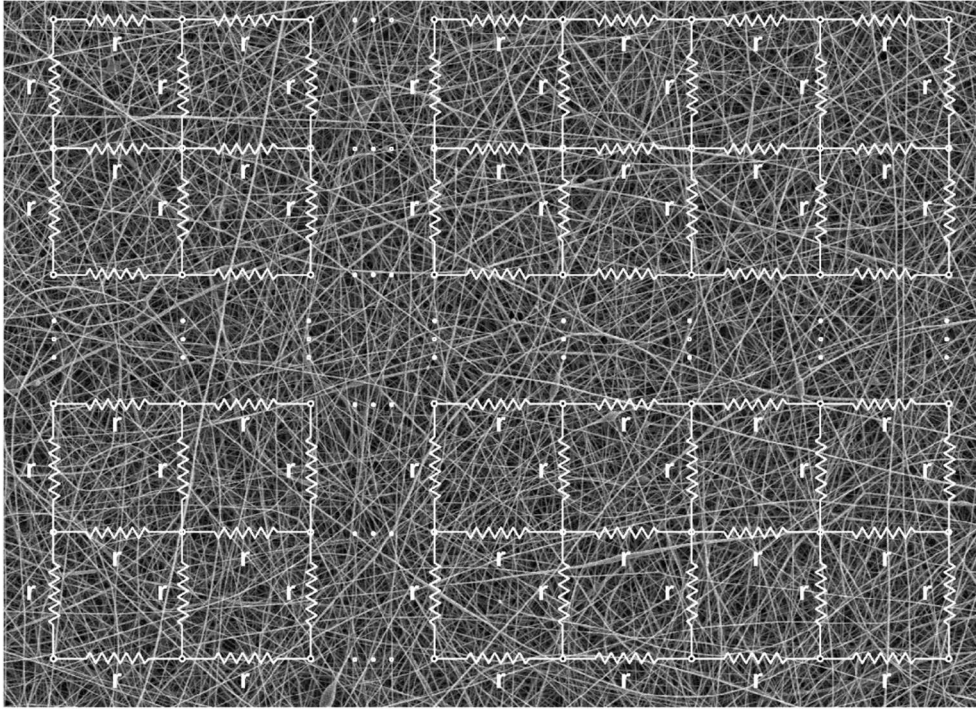
**Supplementary Fig. 5 | Analogy of BioAI<sup>2</sup> to C-LTMRs.** **a** C-LTMR generates spikes due to hair deflection<sup>7</sup>. **b** BioAI<sup>2</sup> generates spikes due to hair deflection. **c** Ion-gated channels within organisms enable information transmission<sup>25</sup> (CC BY 4.0). **d** Leaky IF neuron model. When the potential exceeds a threshold  $\theta$ , a spike is generated<sup>25</sup>. **e** Leaky IF neuron model of BioAI<sup>2</sup>.



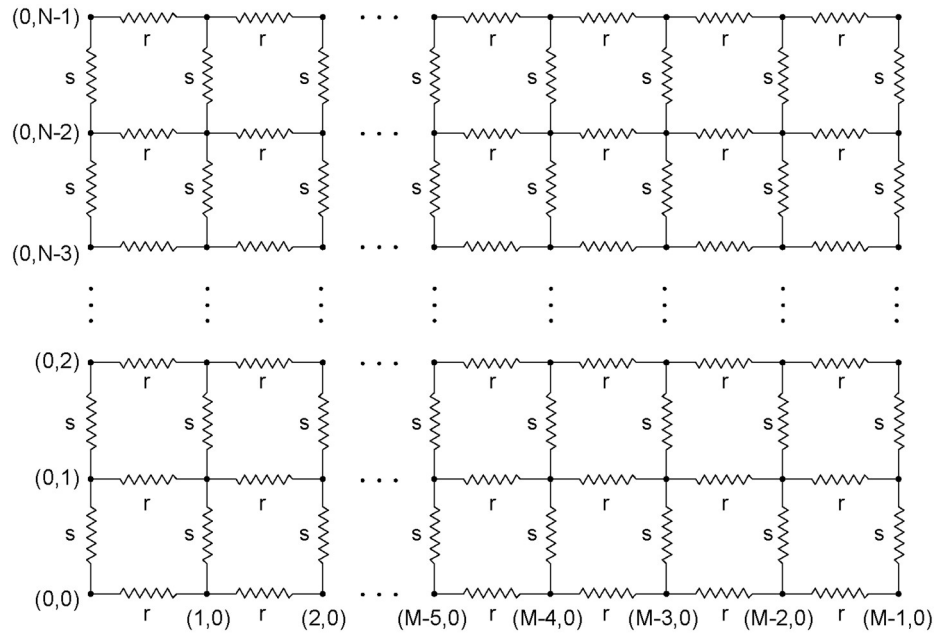
**Supplementary Fig. 6 | Dynamic response of BioAl<sup>2</sup> under different frequencies.**



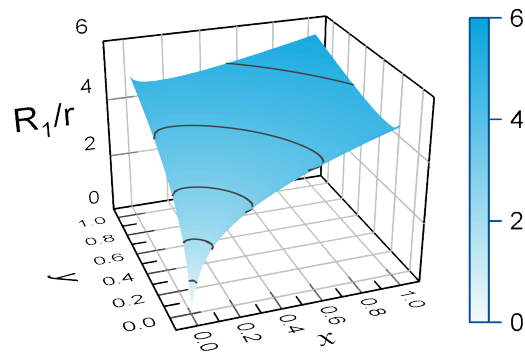
**Supplementary Fig. 7 | Demonstration of position independence of the force measurement.**



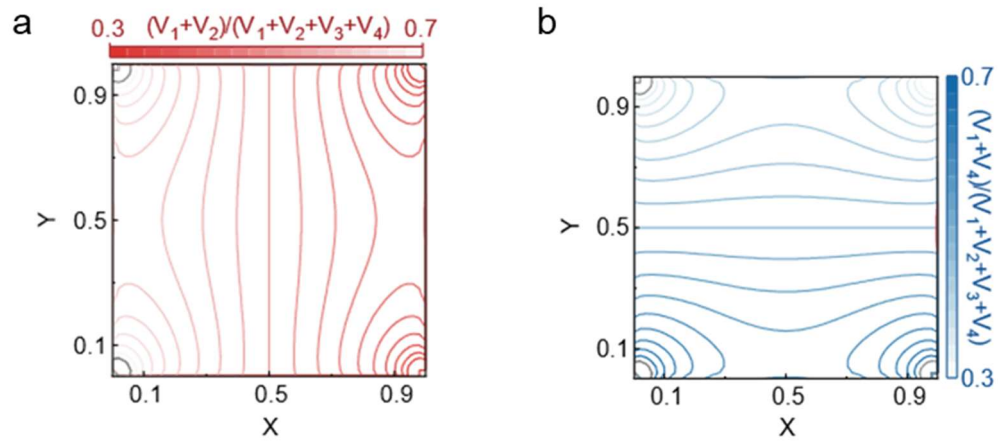
**Supplementary Fig. 8 | Finite boundary rectangular conductive film.**



**Supplementary Fig. 9 | A  $M \times N$  rectangular network.**

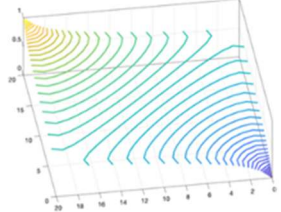
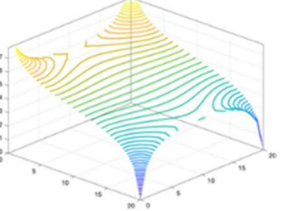
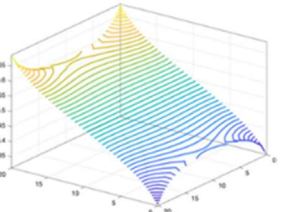


**Supplementary Fig. 10 | Relationship between  $R_1/r$  and the position of touch point  $(x,y)$ .**

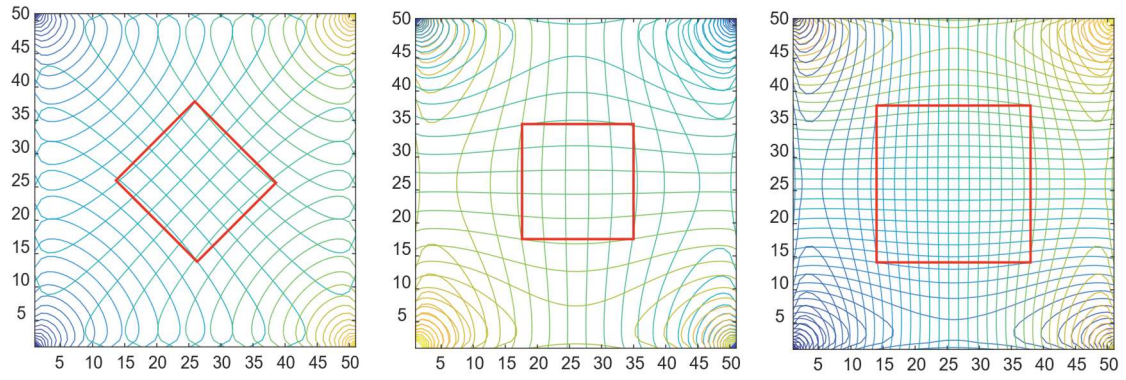


Supplementary Fig. 11 | Isoline derived from the ratio of (a)  $x = \frac{V_1+V_2}{V_1+V_2+V_3+V_4}$  and

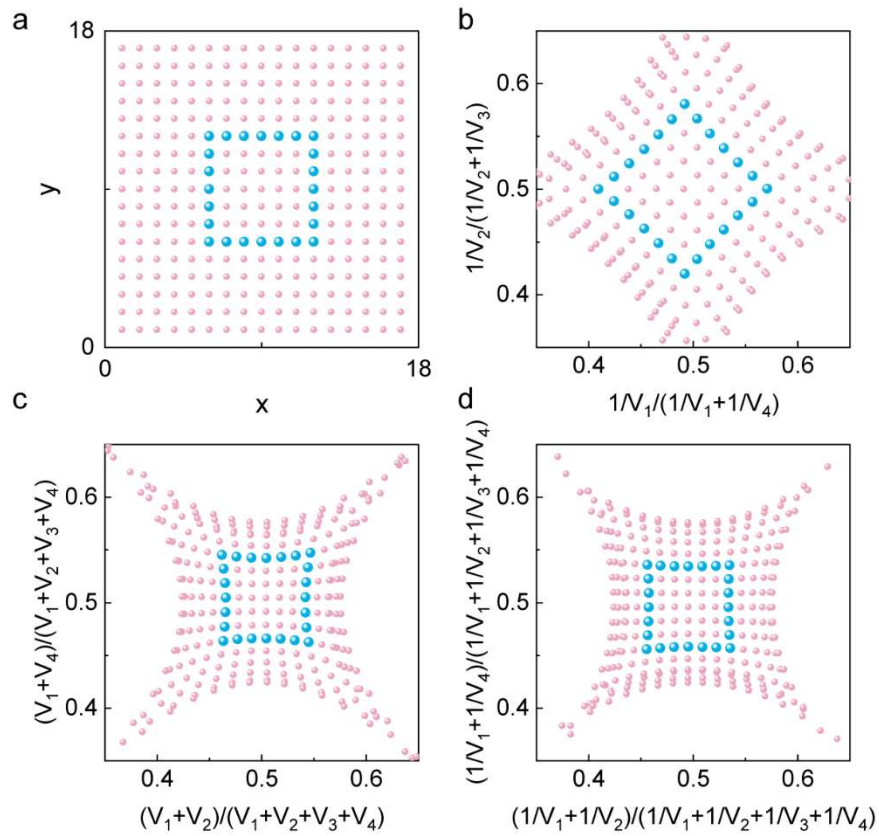
(b)  $y = \frac{V_1+V_4}{V_1+V_2+V_3+V_4}$ .

Equation	Isoline
$\frac{V_1}{V_1 + V_4} \approx \frac{R_4}{R_1 + R_4}$	
$\frac{V_1 + V_2}{V_1 + V_2 + V_3 + V_4} \approx \frac{\frac{1}{R_1} + \frac{1}{R_2}}{\frac{1}{R_1} + \frac{1}{R_2} + \frac{1}{R_3} + \frac{1}{R_4}}$	
$\frac{\frac{1}{V_1} + \frac{1}{V_3}}{\frac{1}{V_1} + \frac{1}{V_2} + \frac{1}{V_3} + \frac{1}{V_4}} \approx \frac{R_1 + R_3}{R_1 + R_2 + R_3 + R_4}$	

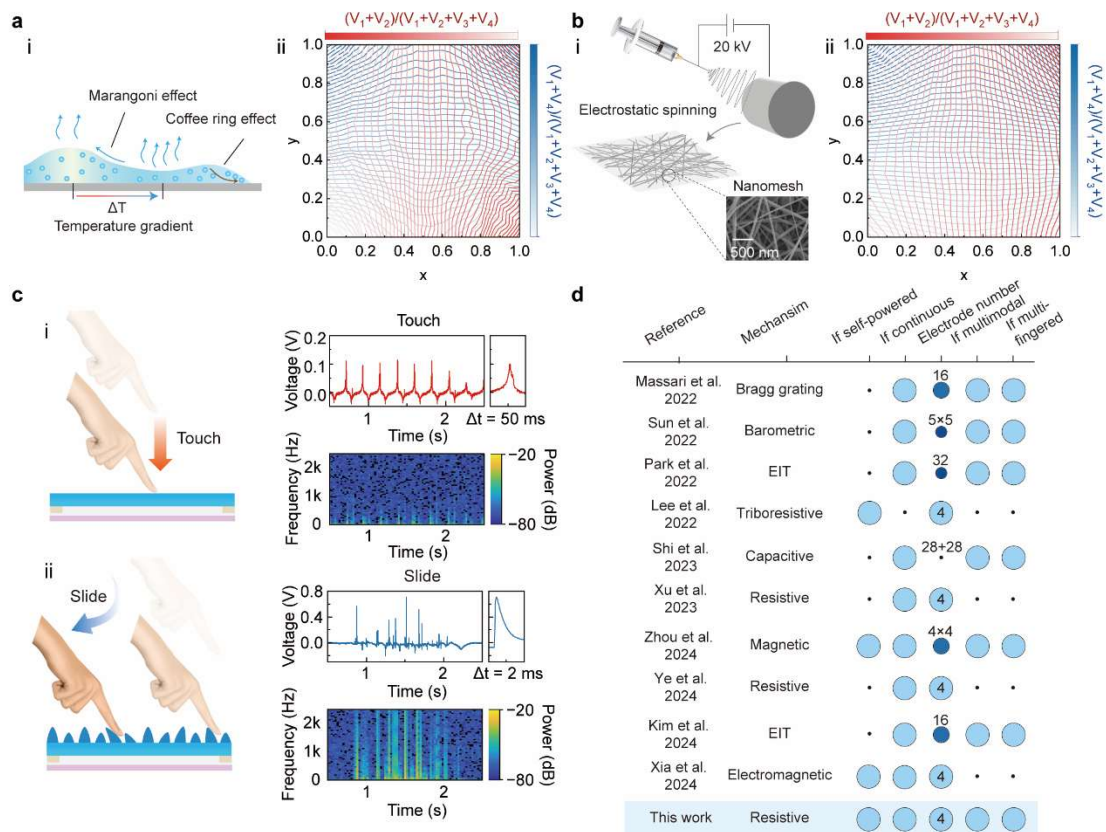
**Supplementary Fig. 12 | Three different calculation formulas for positioning and their isolines (The number of contour lines is unified).**



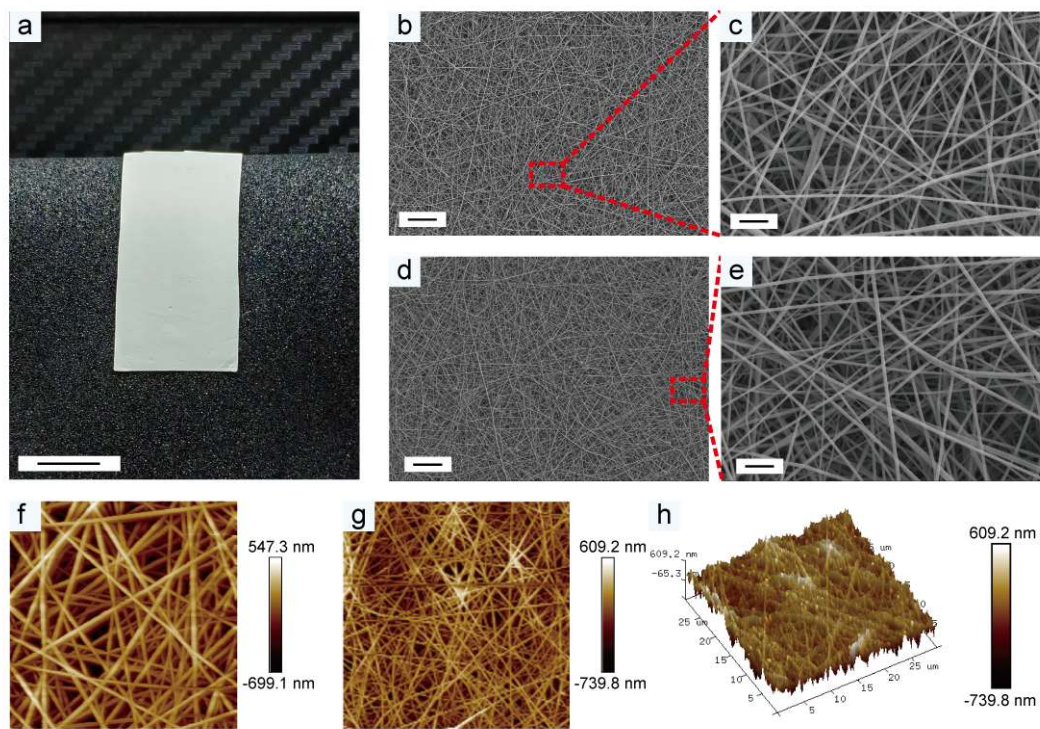
**Supplementary Fig. 13 | Calculated isoline of equations in Supplementary Fig. 11.** The red square indicates the near linear area, from which it can be found that the third methods present the largest near-linear area. The number of contour lines is unified.



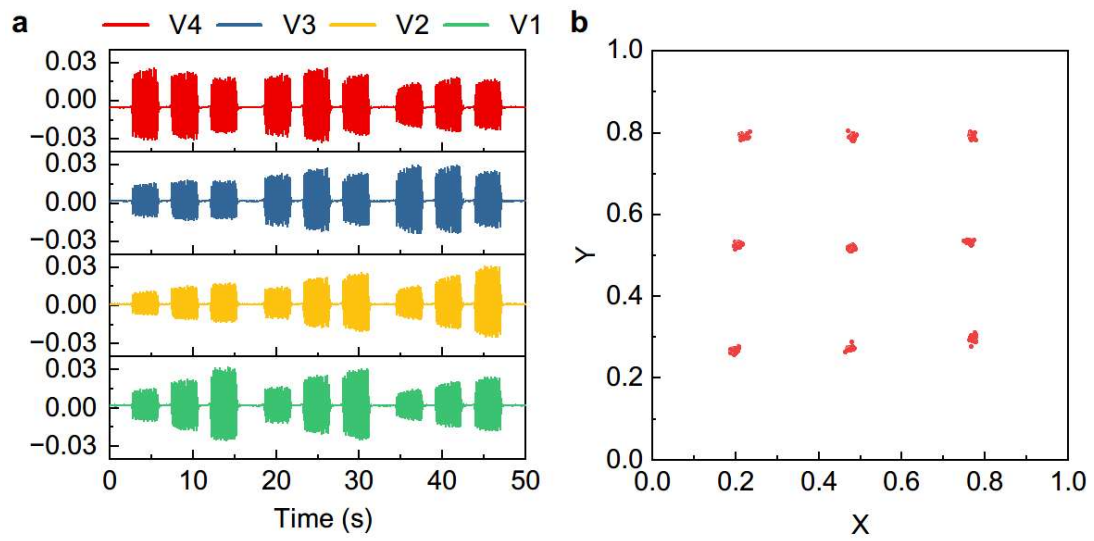
**Supplementary Fig. 14 | Illustration of the distortion caused by different calculated equations.** **a** Reference touch positions (pale red) and a square (blue). **b-d** The corresponding positions calculated by equations in Supplementary Fig. 12. The results reveal that the third square presents minimal distortion which is in agreement with the conclusion in Supplementary Fig. 13.



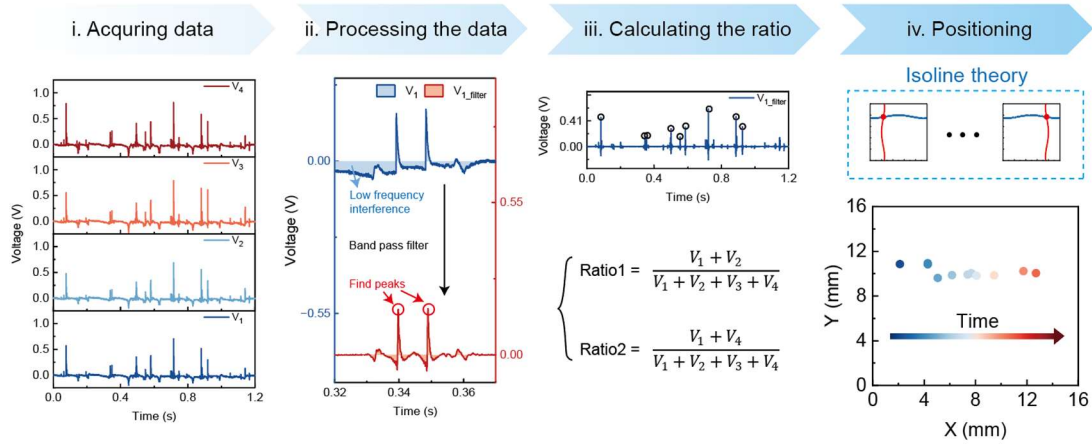
**Supplementary Fig. 15 | Illustration of the positioning ability of the BioAI<sup>2</sup>.** **a** (i) Illustration of volatilization of a liquid film. During the evaporation process, due to the influence of external conditions such as humidity and airflow, there exist differences in evaporation rates across various regions of the liquid surface. This leads to variations in temperature and concentration within different areas of the liquid, resulting in discrepancies in surface tension. Such discrepancies trigger the Marangoni effect, which causes uneven material flow and subsequently results in uneven thickness in the cured film. Additionally, the coffee-ring effect is also present at the edge of the liquid surface, causing the film thickness at the edges to be thicker. These effects collectively contribute to the significant thickness inhomogeneity observed in the solidified film. (ii) The measured isoline distribution of the conductive layer fabricated by volatilization of a liquid film. **b** (i) Illustration of a conductive layer by electrostatic spinning. The SEM images are shown in Supplementary Fig. 16. (ii) The measured isoline distribution of the conductive layer fabricated by electrostatic spinning. **c** Illustration of the triboelectric signals and corresponding time-frequency diagram generated from (i) a traditional plane interface and (ii) the proposed BioAI<sup>2</sup>. **d** Comparison with other excellent works on the cutting edge<sup>26-35</sup>.



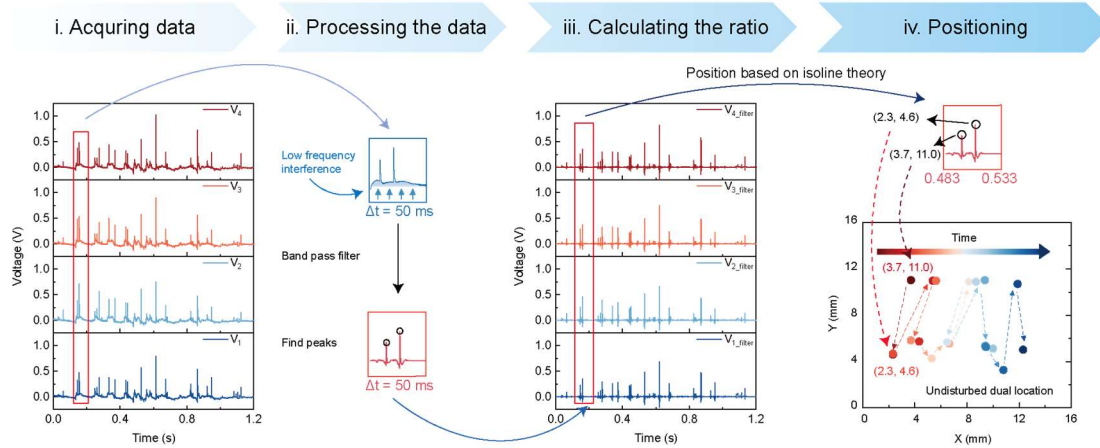
**Supplementary Fig. 16 | Surface topography characterization of the fabricated conductive layer.** **a** Photograph of the conductive layer. **b** Scanning electron microscope image (SEM) of the conductive layer. **c** Enlarge view of the image in **b**. **d** SEM image of the conductive layer in another part of the membrane. **e** Enlarge view of the image in **d**. (Scale bars: 1 cm (**a**), 5  $\mu\text{m}$  (**b**), 500 nm (**c**), 5  $\mu\text{m}$  (**d**), 500 nm (**e**.) The thickness and distribution of fibers in (**b,c**) and (**d,e**) are similar which indicates that the fabricated conductive layer is relatively uniform. **f-h** Atomic force microscope image (AFM) of the conductive layer.  $R_a = 150$  nm. (Scale bars: 2  $\mu\text{m}$  (**f**), 6  $\mu\text{m}$  (**g**)). The AFM reveals that the difference in height of the conductive layer is lower than 1.5  $\mu\text{m}$ . Similar results were observed in two independent experiments.



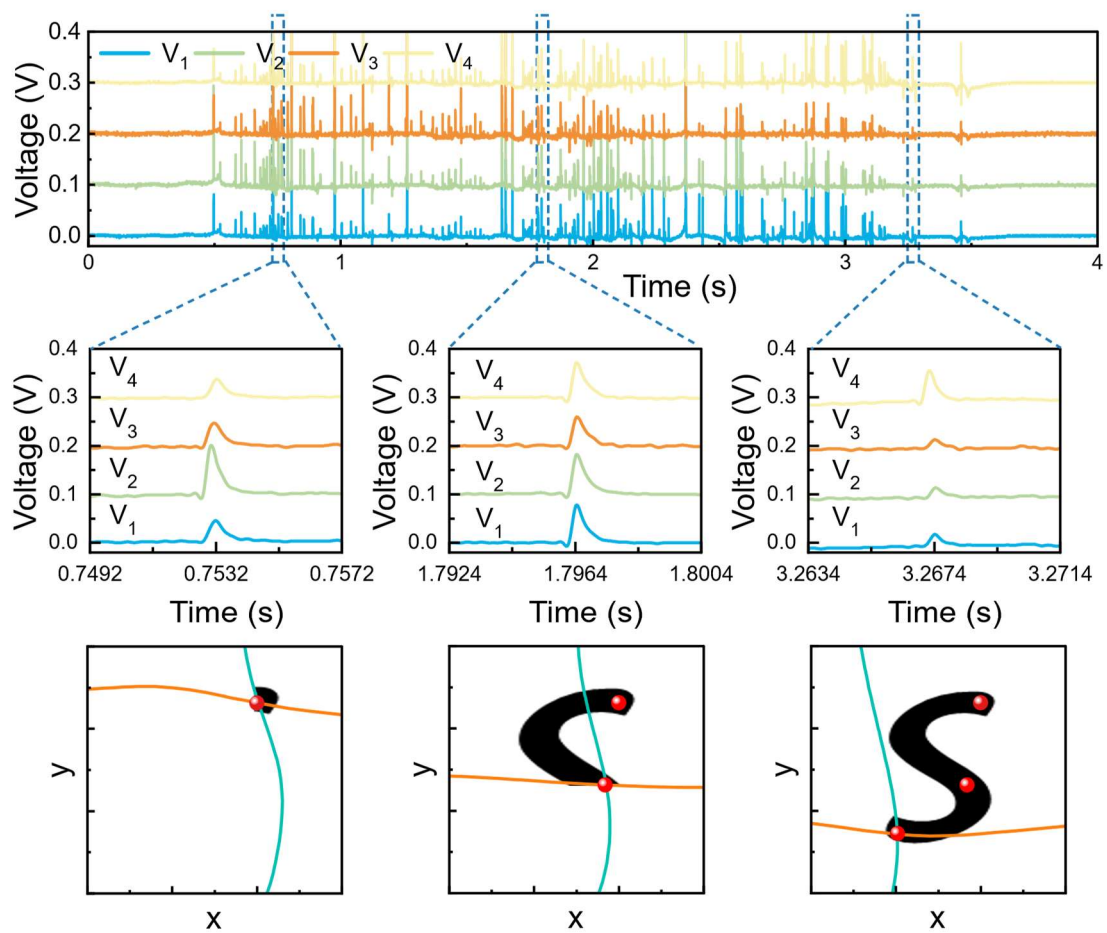
**Supplementary Fig. 17 | Positioning repeatability testing.** **a** Voltage output of four electrodes when touching the BioAI<sup>2</sup> at different positions more than 30 times. **b** Corresponding calculated positions which verify the reproducibility of the position methods.



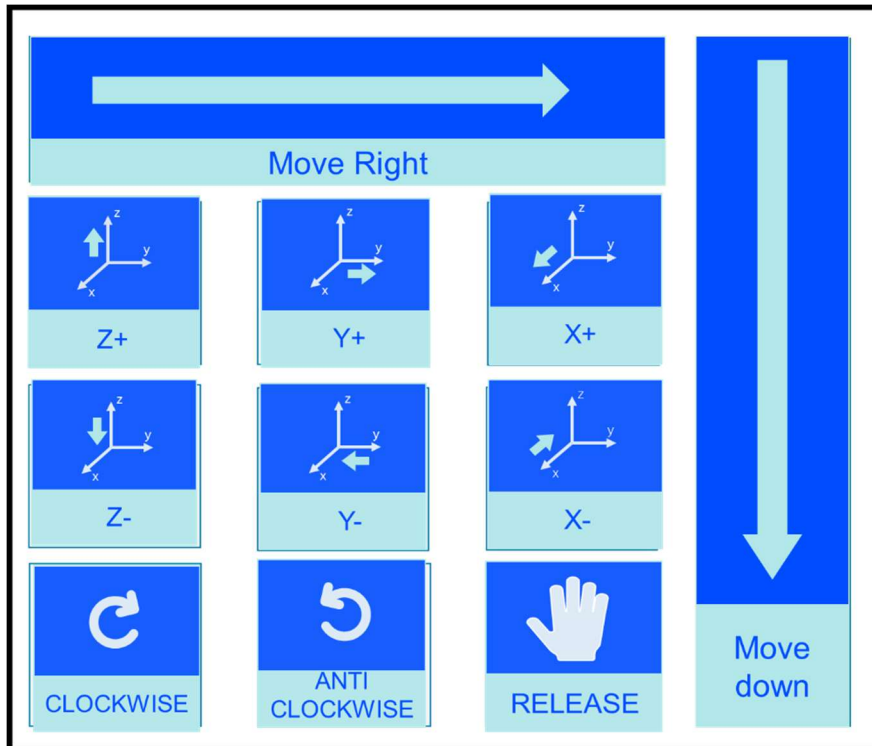
**Supplementary Fig. 18 | Single finger stroking trajectory positioning ability.** (i) First, collect the sliding data; (ii) Second, in order to avoid the interference of the low-frequency signal, the bandpass filter is carried out, and then the signal pulse peak is found; (iii) Third, after finding suitable peaks on four signals, the ratios in equation (3) and (4) are then calculated; (iv) In the fourth step, the stroking trajectory points are obtained based on the ratios and the isoline theory. According to the result, attributed to the super-high temporal resolution of the spike-like signals, the trajectory points from a single finger can be reconstructed continuously.



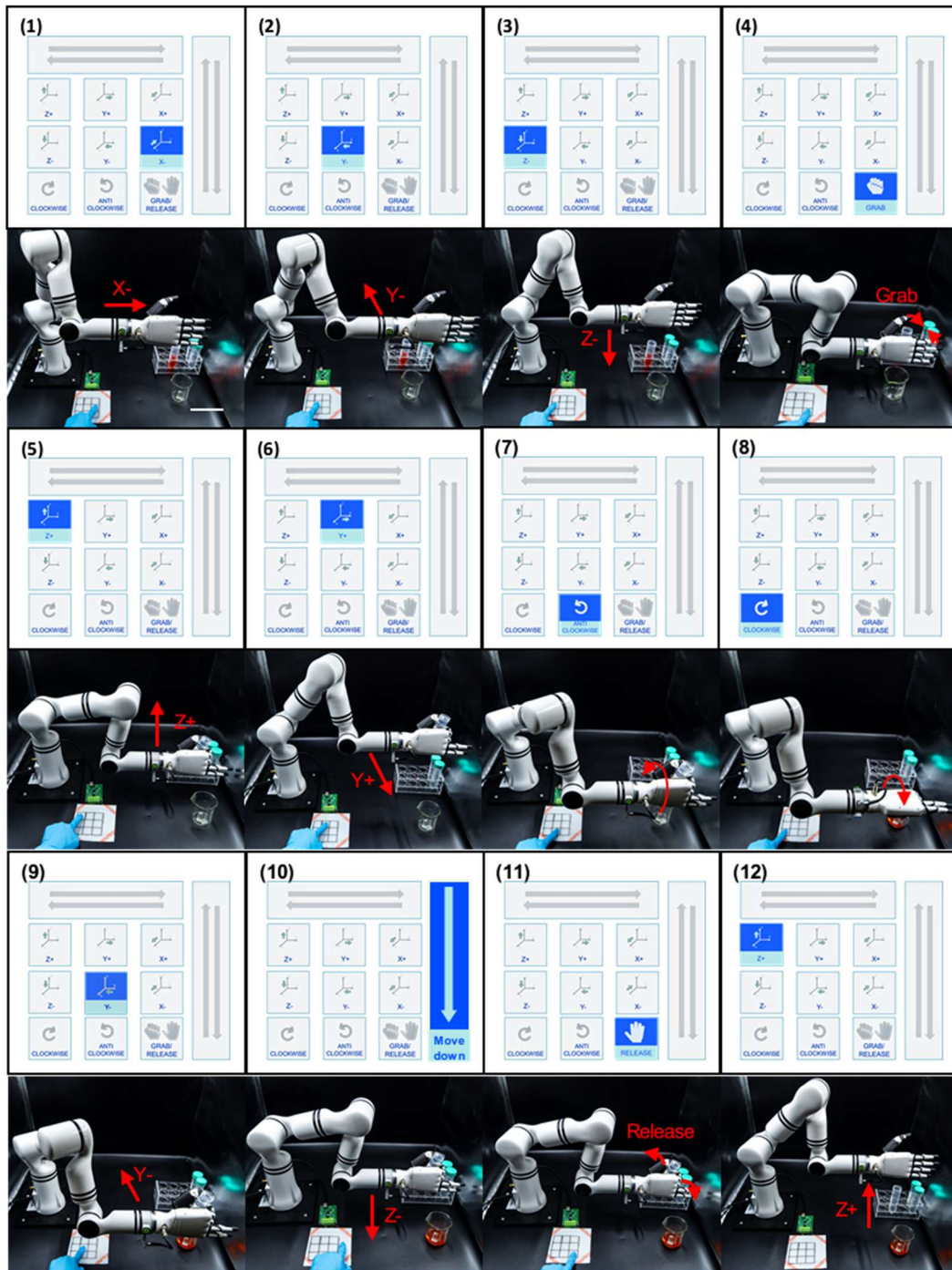
**Supplementary Fig. 19 | Multi-finger stroking trajectory positioning ability.** (i) First, collect the sliding data; (ii) Second, in order to avoid the interference of the low-frequency signal, the bandpass filter is carried out, and then the signal pulse peak is found; (iii) Third, after finding suitable peaks on four signals, the ratios in equation (3) and (4) are then calculated; (iv) In the fourth step, the stroking trajectory points on the two fingers are obtained based on the ratios and the isoline theory. According to the result, attributed to the super-high temporal resolution of the spike-like signals, the trajectory points from two fingers will not influence each other.



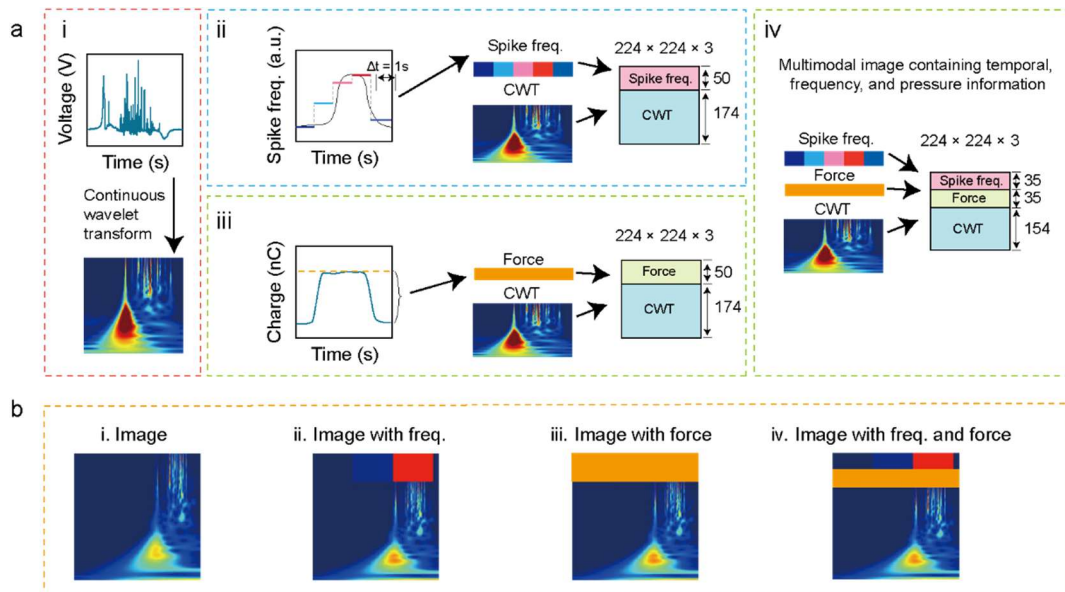
**Supplementary Fig. 20 | Illustration of the voltage signal outputs during sliding an S pattern on the BioAI<sup>2</sup> (top) and the corresponding isolines (bottom).**



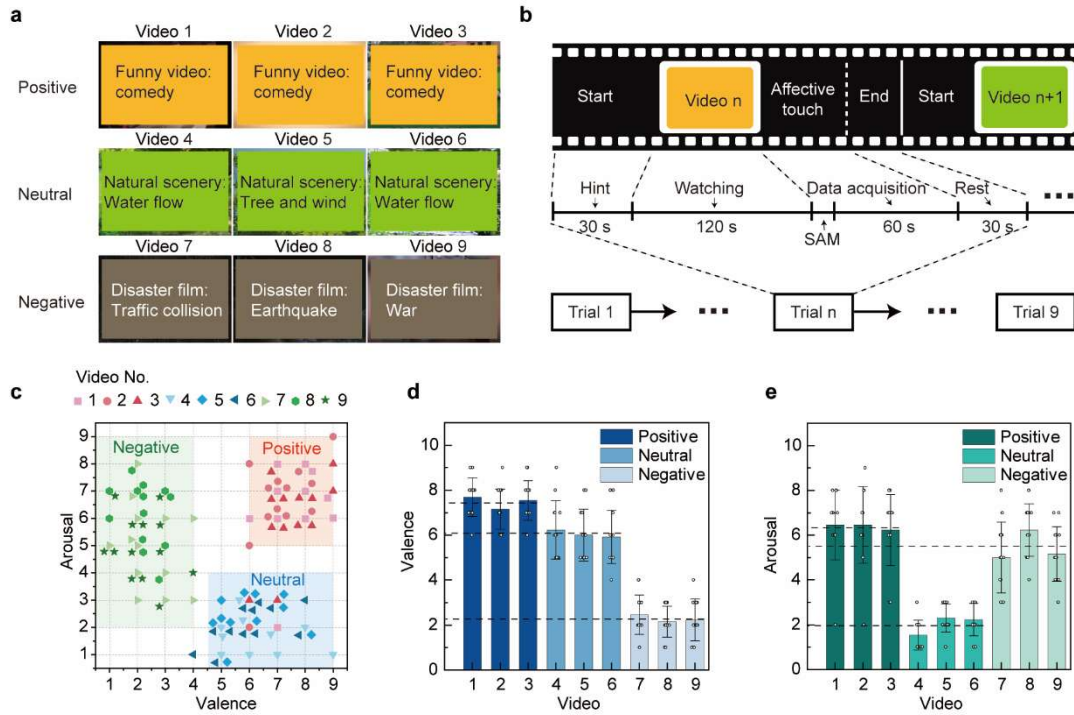
**Supplementary Fig. 21 | Illustration of the functions of the touchpad on different positions.** Here, the functions of move right/left and move down/up are triggered by sliding on the interface.



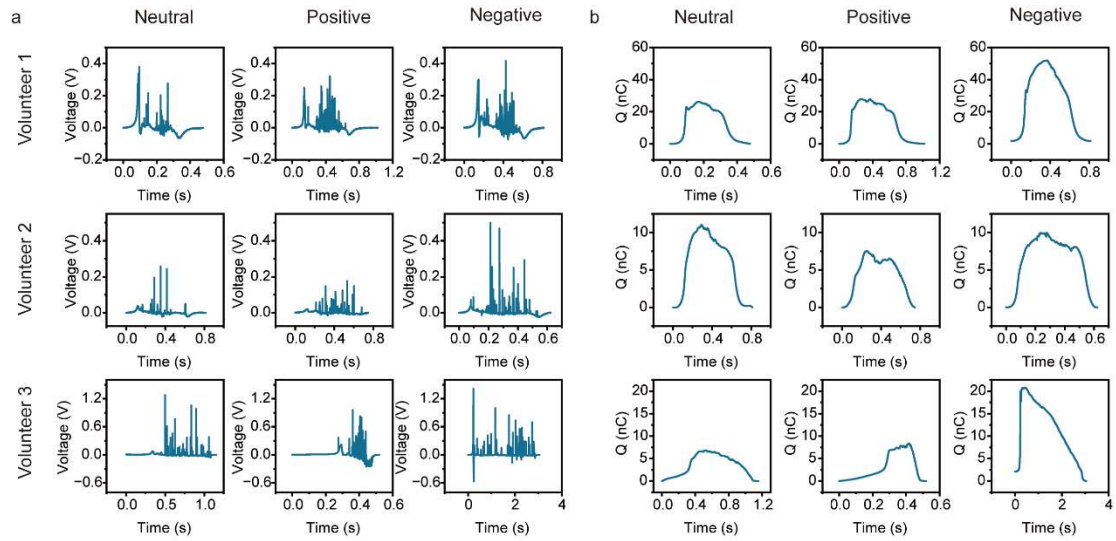
Supplementary Fig. 22 | Illustration of the actions of the robot hand and arm when the touchpad is touched in different positions. Scale bar: 10 cm.



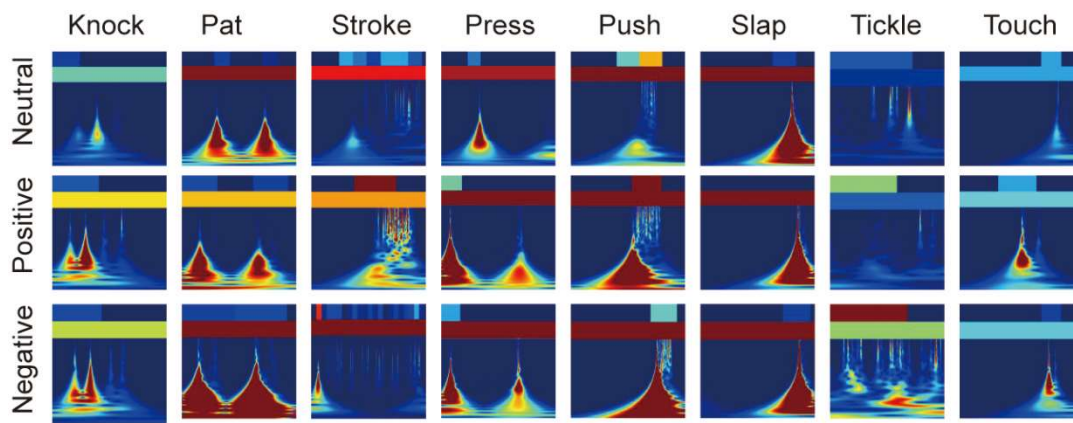
**Supplementary Fig. 23 | Illustration of the process methods of the image input. a** There are four types of image inputs for the neural network. (i) The first type of image is obtained through the continuous wavelet transform of voltage signals to extract the temporal information from data. (ii) The second input consists of the CWT result and the magnitudes of the spike frequency which are calculated every 1 s and are rendered as different colors at the top part of the image. (iii) The third input adds the amplitude of the force to the first input. (iv) The fourth input integrates multimodal information (temporal, frequency and pressure information). **b** Some samples of image processed by the above methods.



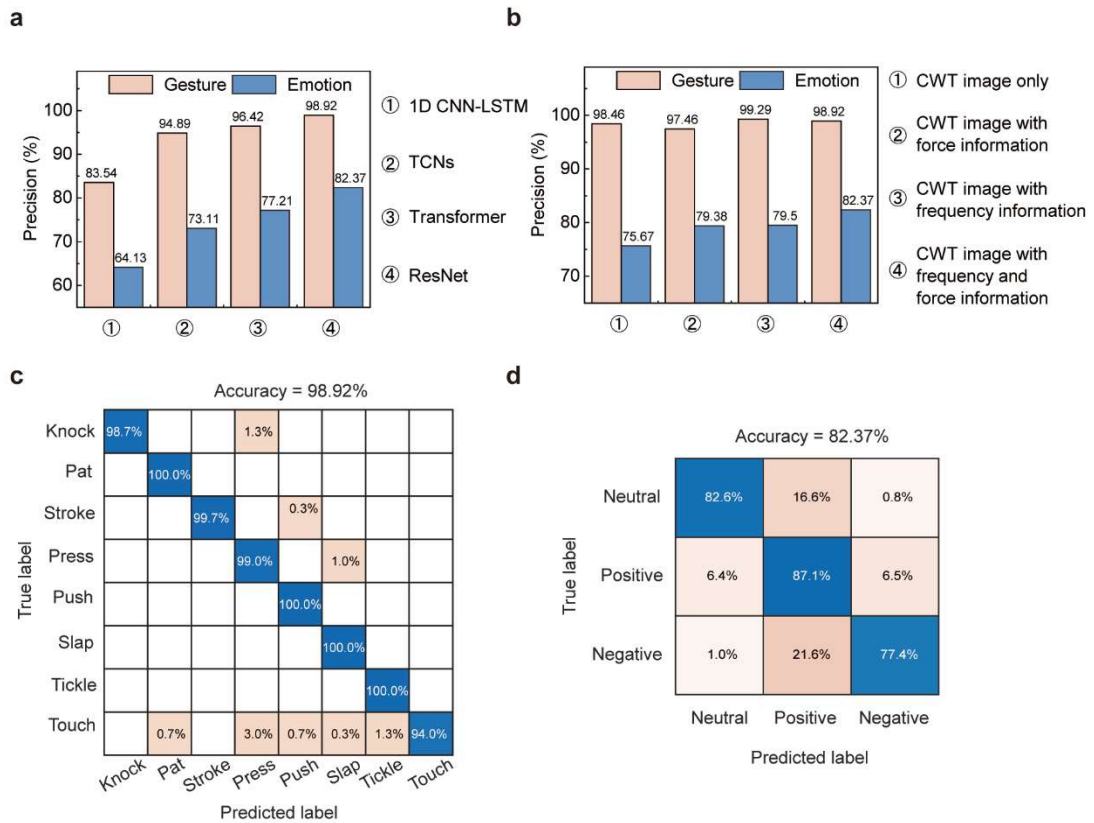
**Supplementary Fig. 24 | Effectiveness validation of the emotion evoking videos.** **a** Nine video clips for the emotion experiment. Video no. 1-3 for positive, 4-6 for neutral, 7-9 for negative. **b** Protocol used in the emotion experiment. Here, in every trial, the experimenter first received a hint which showed the gestures required to do. Then, a 2-min video was played. When the video ended, the experimenter needed to finish a SAM questionnaire (Supplementary Fig. 34) and perform three different gestures on the BioAI<sup>2</sup>. Each action lasted 20 seconds. At last, the experimenter rested for 30 seconds to calm down. **c** Rating distributions of different film clips from 13 participants on the arousal-valence plane. **d,e** Mean ratings for arousal (**d**) and valence (**e**) (Data are mean +/- SD, n = 13).



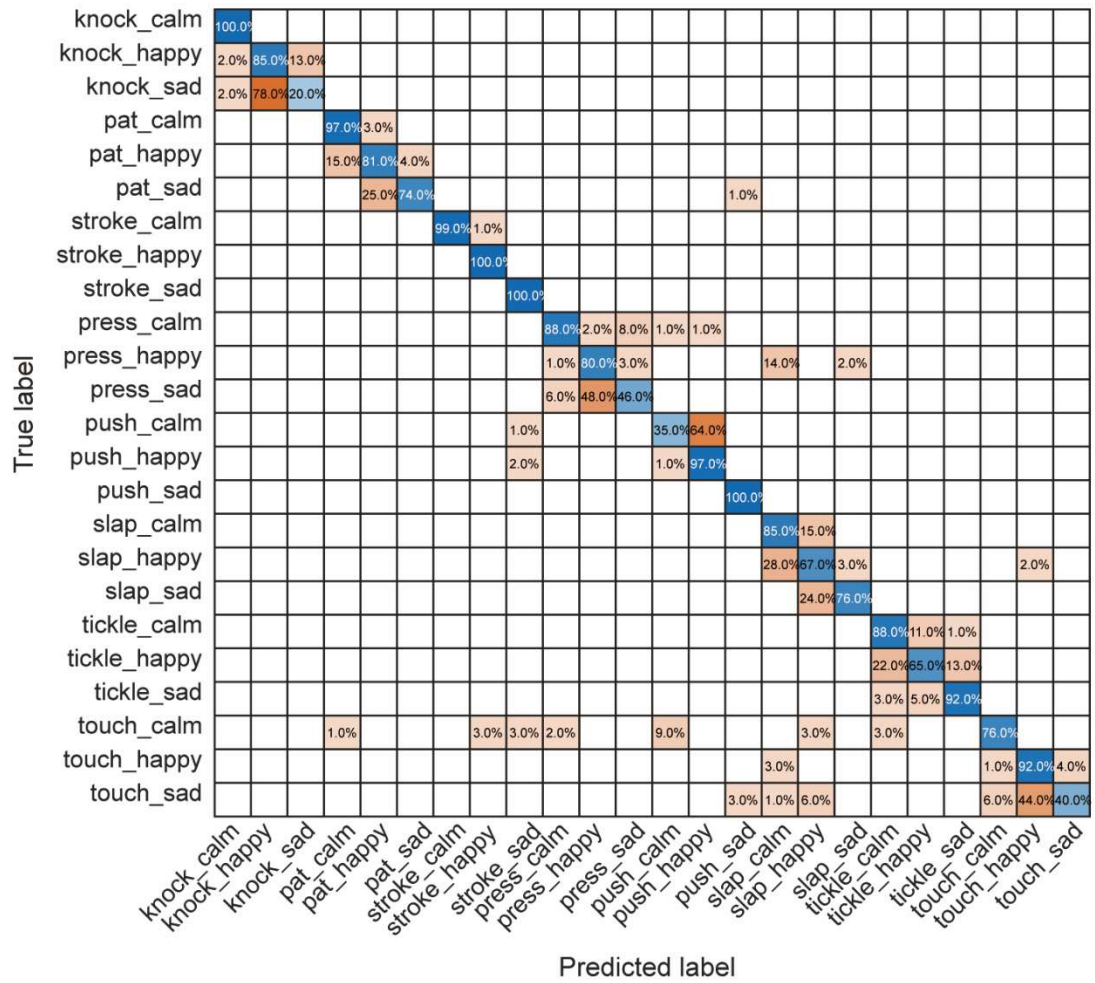
**Supplementary Fig. 25 | Voltage (a) and charge (b) outputs from different volunteers with different evoked emotions and the same gesture (stroke). The data reveals the diversity of the tactile data from different volunteers.**



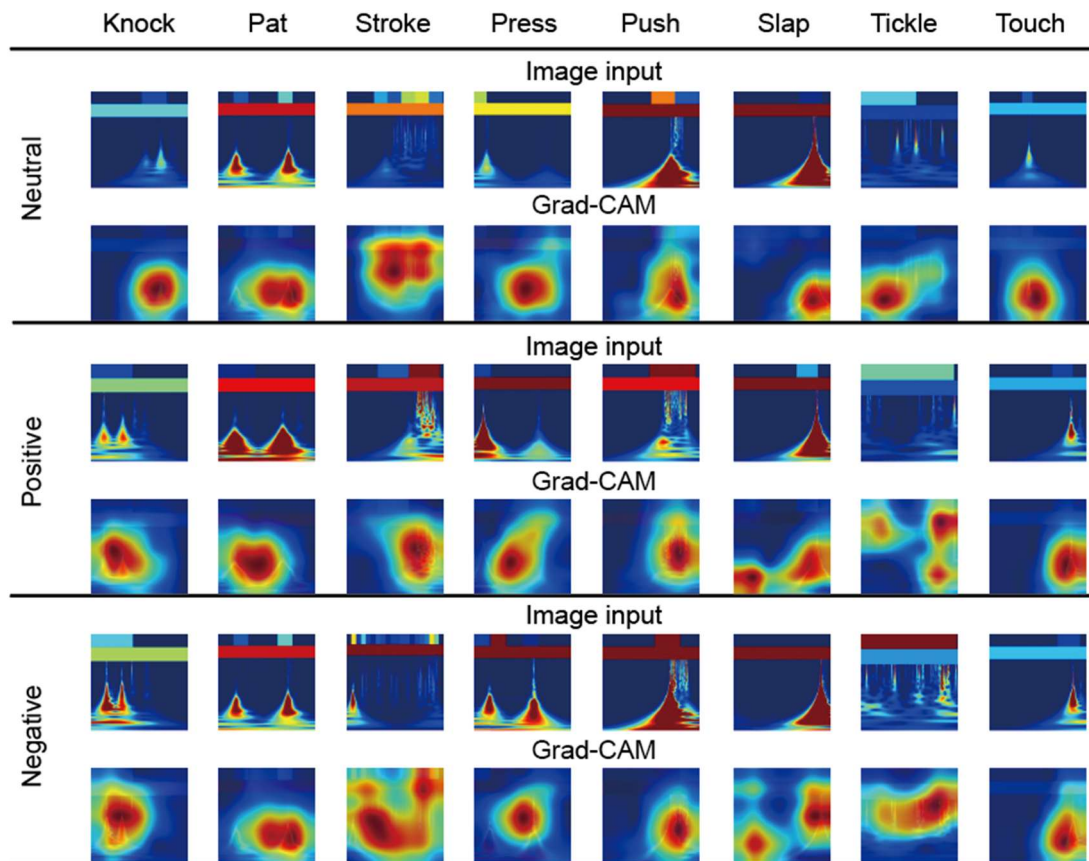
**Supplementary Fig. 26 | Some samples of the processed images.**



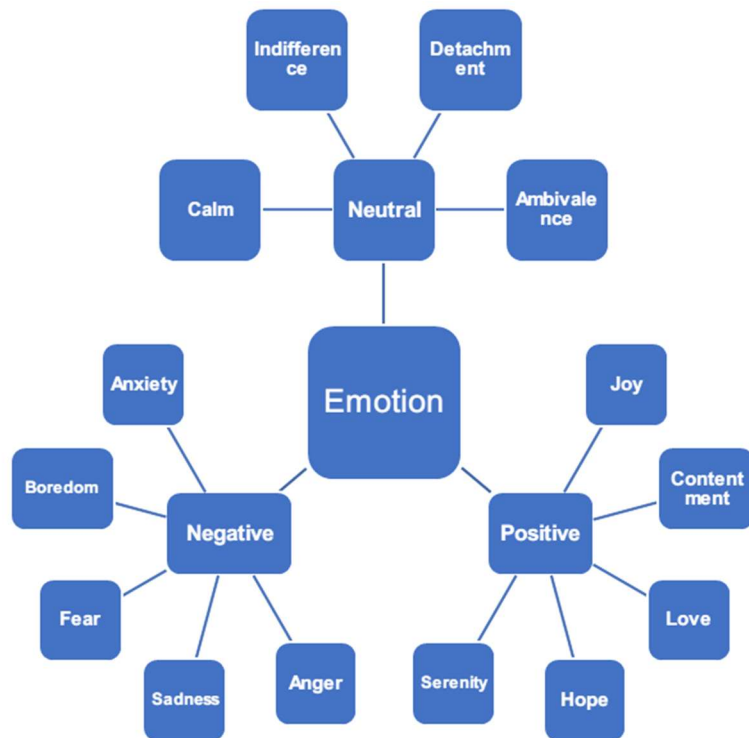
**Supplementary Fig. 27 | Comparison of the precision of gesture and emotion recognitions between different neural network settings. a** Comparison between different neural network structures (1D CNN-LSTM, TCNs, Transformer and ResNet). **b** Comparison between different neural network image settings. The findings revealed that frequency information was vital for both tasks. Interestingly, force information, while slightly reducing the performance on the isolated gesture recognition task, provided a substantial positive contribution to the accuracy of emotion recognition. This indicates that the physical force of an interaction carries important affective cues. The model utilizing the combined frequency and force information achieved the highest overall emotion recognition performance. **c,d** Confusion matrix for gestures (**c**) and emotion (**d**) recognition of CNN inputted with CWT images, frequency information and force information.



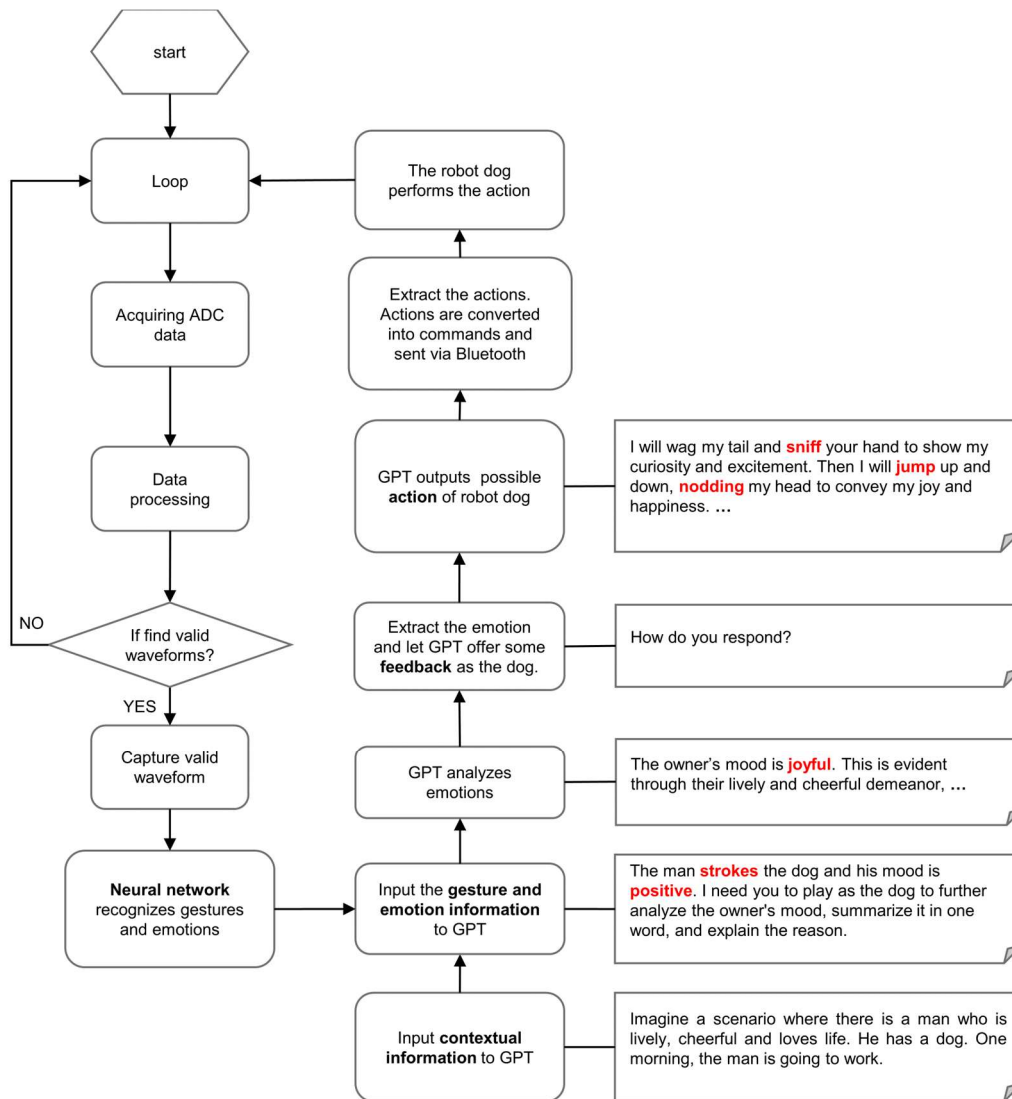
**Supplementary Fig. 28 | Complete confusion matrix for 24 labels (8 gestures × 3 emotions).**



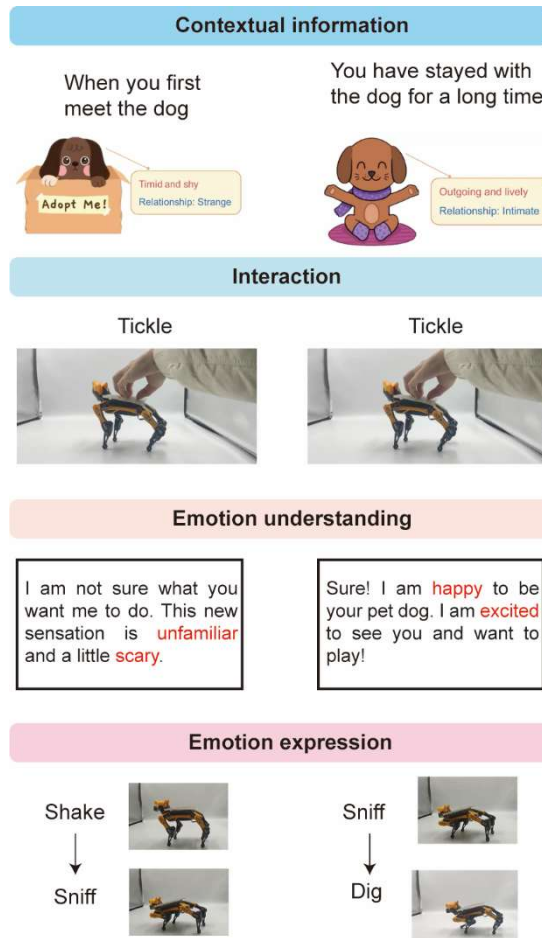
Supplementary Fig. 29 | Original image input with different gestures and emotion label and their corresponding Grad-CAM for the applied CNN.



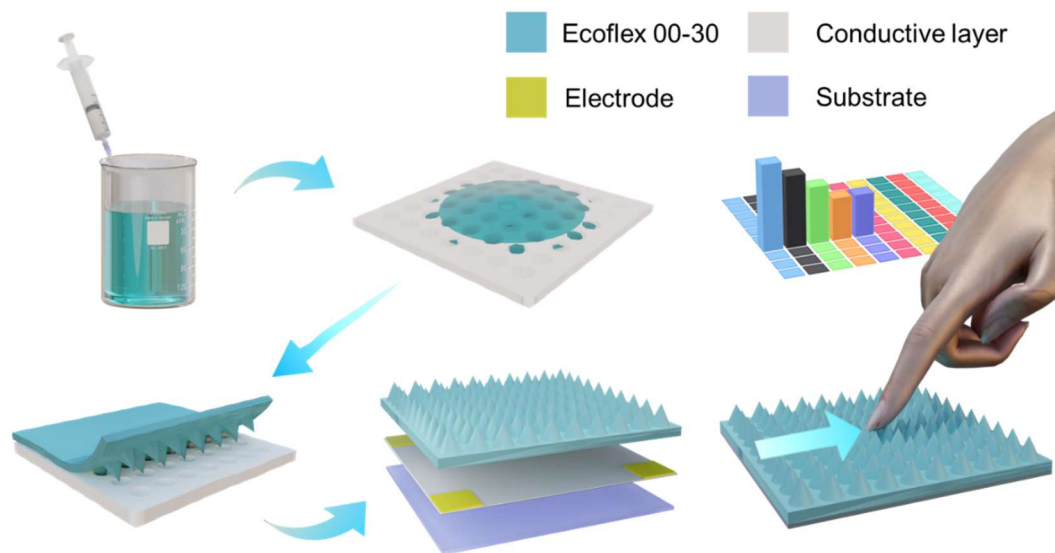
**Supplementary Fig. 30 | Emotion neural topology diagram.** It shows a part of the potential sub-emotions that can be derived from the three main emotions (Neutral, positive negative).



**Supplementary Fig. 31 | Working flow of the emotional interaction process.**

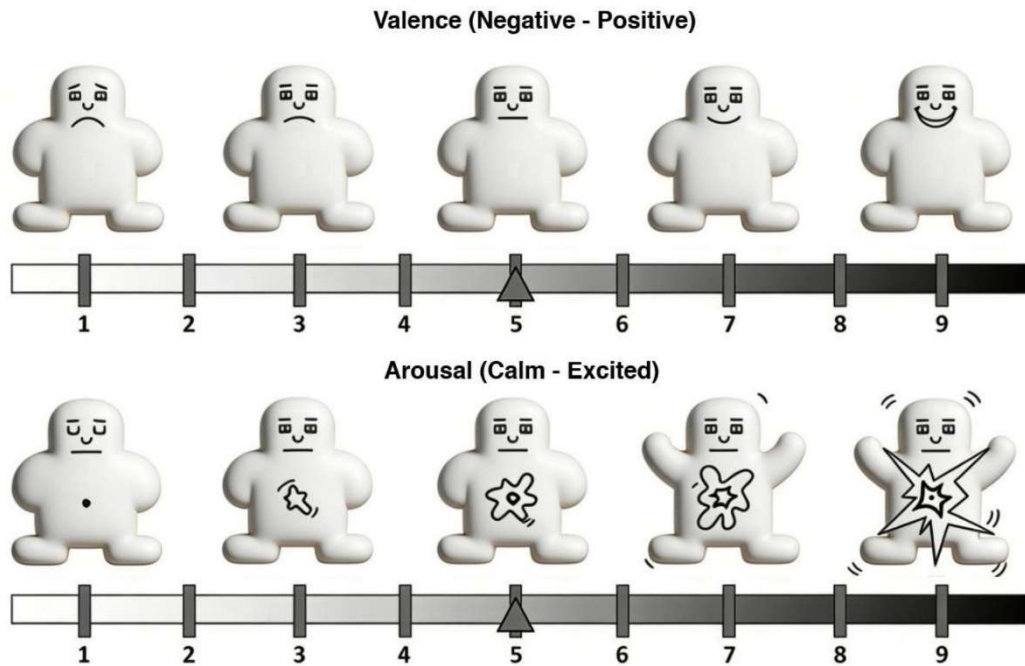


**Supplementary Fig. 32 | Flowchart illustrating the impact of the context information on the understanding and expression of emotions.** Here, two different context information (scenario, characteristics of the dog, and the relationship between human and dog) were set and the same interaction (tickle) was applied to the BioAI<sup>2</sup>. The ChatGPT presented different emotion understanding and executed different actions to express different emotions.



**Supplementary Fig. 33 | Fabrication process of the BioAI<sup>2</sup>.**

- The first dimension is valence, which measures positive and negative emotions. 9 for "very pleasant", 5 for "neutral", and 1 for "very unpleasant".
- The second dimension is arousal, which represents the degree to which emotions are aroused, and mainly measures the strength of emotions. 9 for "very excited", 5 for "neutral", and 1 for "very calm".



Name:

Age:

Gender: Male  / Female

Video Emotion	No. 1	No. 2	No. 3	No. 4	No. 5	No. 6	No. 7	No. 8	No. 9
Valence									
Arousal									

**Supplementary Fig. 34 | SAM<sup>21</sup> questionnaire used during the emotion-evoking experiments.**

Supplementary Table 1. State-of-the-art soft electronics for tactile mapping interface

Works	Methods	Inter-connect free	Energy supply free	Multi-point mapping	Sensing area (mm <sup>2</sup> )	Electrode number	Pixel number	Temporal resolution /refresh rate	Sensing range
Kim et al. <sup>36</sup>	Multiscale structures	×	×	○	25	6	25	24 ms	16-80 kPa
Oh et al. <sup>37</sup>	Transistor arrays	×	×	○	600	25	128	10 ms	0-5 kPa
Huang et al. <sup>38</sup>	Capacitive sensor arrays	×	×	○	625	10	25	N/A	20-35 kPa
Zhong et al. <sup>39</sup>	Transistor arrays	×	×	○	8	>20	200	N/A	N/A
Shi et al. <sup>30</sup>	Capacitive sensor arrays	×	×	○	10,000	56	784	120 Hz	0.15-440 kPa
Park et al. <sup>28</sup>	EIT, PAT	×	×	○	40,000	32(EIT) +25(PAT)	~2268*	N/A	N/A
Cho et al. <sup>40</sup>	Resistive and capacitive	○	×	×	10,000	2	16,891	N/A	N/A
Lee et al. <sup>41</sup>	Triboresistive	○	○	×	1,200	4	9	N/A	N/A
Xu et al. <sup>31</sup>	Resistive	○	×	×	10,000	4	100	70 ms	N/A
Xia et al. <sup>35</sup>	Resistive	○	○	×	3,600	4	49	N/A	N/A
Kim et al. <sup>34</sup>	EIT	○	×	○	314	16	>920	N/A	3.2-159 kPa
Massari et al. <sup>26</sup>	Fibre Bragg grating.	○	×	○	>10,000	16	16	N/A	0-2.5 N
Our work	Biomimetic hairy based triboresistive	○	○	○	10,000	4	3858*	5 ms	0-50 N

○ denotes Yes, × denotes No.

\* Calculated by  $S/(\delta)^2$ , S denotes the sensing area,  $\delta$  denotes root mean square (RMS) error.

EIT: Electrical impedance tomography.

PAT: Passive acoustic tomography.

Supplementary Table 2 Parameter used in simulation

Dielectric	$\epsilon_0 = 1, \epsilon_r = 3, \epsilon_0 = 8.854 \cdot 10^{-12}, d_1 = 100 \mu\text{m}$
Tribo-charge surface density	$\sigma = 8 \mu\text{C m}^{-2}$
Size of electrode	$S = 10 \text{ mm}^2$
Capacitor	$C_D = 200 \text{ pF}, C_E = 10 \text{ pF}$
Contact area	$S(t)$ , calculated by simulation

Table 3 Comparison between BioAI<sup>2</sup> and biological C-LTMRs

<b>Response Characteristic</b>	<b>BioAI<sup>2</sup> Performance</b>	<b>Biological LTMRs (Literature)</b>	<b>C- Biomimetic Significance</b>
<b>Optimal Stroking Speed</b>	30 - 80 mm/s	Prefer slow speeds (e.g., 1-10 cm/s)	Both are tuned to velocities associated with affective, non-discriminative touch.
<b>Effective Speed Range</b>	0 - 300 mm/s	0 - 300 mm/s	Both operate within a defined dynamic range of gentle mechanical stimuli.
<b>Response Curve Shape</b>	Inverted shaped	U- shaped	U- The non-monotonic response is a key functional signature of C-LTMRs, which BioAI <sup>2</sup> successfully replicates.

Furthermore, the BioAI<sup>2</sup>'s response curve can be modulated by structural parameters (e.g., hair height, stiffness, spacing), which alter the capacitive coupling and charge transfer dynamics (as described by Equation (13)-(17)). This tunability mirrors the biological variability and adaptation found in sensory systems and allows us to engineer the device's specific response profile to closely match that of C-LTMRs.

Supplementary Table 4 Comparison between different networks on emotion recognition

<b>Method</b>	<b>Action recognition accuracy</b>	<b>Affection recognition accuracy</b>	<b>Total recognition accuracy</b>
1D CNN & LSTM (Waveform with voltage and charge information)	83.54%	64.13%	61.56%
TCNs (Waveform with voltage and charge information)	94.89%	73.11%	71.14%
ResNet (CWT image only)	98.46%	75.67%	75.67%
ResNet (CWT image with force information)	97.46%	79.38%	78.46%
ResNet (CWT image with frequency information)	<b>99.29%</b>	79.50%	79.13%
ResNet (CWT image with frequency and force information)	98.92%	<b>82.37%</b>	<b>81.92%</b>
Transformer (CWT image with frequency and force information)	96.42%	77.21%	76.62%

Supplementary Table 5 State of the art for affective touch perception

Works	Touch object	Touch data	Gestures	Emotion elicitation and classification	Emotion types	Number of data subjects	Automatic detection algorithm	Gesture recognition performance	Emotion recognition performance
Shapiro et al. <sup>1</sup>	A silicon ball covered with fabric pressure sensors	Pressure	Squeeze, hold and shake, stroke, ...	×	Anxiety, angry, sad, tentative, certain, positive emotion	16	Autoencoder, MLP	×	2.78 (average MSE, 0-99 scale)
Baldacci et al. <sup>2</sup>	Smartphone	Touch movements	×	DASS	Depression, anxiety, stress	115	Decision tree, RF	×	73.4-74.1%
Wampler et al. <sup>3</sup>	Smartphone	Touch time, position	×	Chat conversations/SAM	Anger, happiness, sadness, surprise, stress	70	Pretrained variational autoencoder, MLP	×	86%
Qi, et al. <sup>5</sup>	Rigid keyboard	Pressure, position	×	IADS	Happiness, fear, disgust, sadness	9	RF	×	78.3%
Niewiadomski et al. <sup>6</sup>	Rigid cube covered	Touch position, kinematics data	Touch, rotate	Imagination	Anger, sadness, excitement and gratitude.	11	SVM, LMKL	×	75%
Flagg et al. <sup>9</sup>	A plastic skeleton with fabric pressure sensors	Pressure, position	Stroke, scratch, squeeze, pat, rub, pull, contact without movement, no touch	×	×	16	RF, NN, LR, and Bayesian networks	86%	×
Jung et al. <sup>10</sup>	A mannequin arm.	Pressure, position	Grab, hit, pat, massage, pinch, poke, press, rub, scratch, squeeze, slap, stroke, tap, tickle	×	×	31	SVM, Bayesian classifier	54%	×
Ku et al. <sup>12</sup>	Rigid robot	Pressure, vibration, position	Stroke, hit, rub, press, touch, no interaction	×	×	5	HMM, LSTM, CNN	87.8%	×
Li et al. <sup>13</sup>	Rigid social robot	Pressure, position	Hit, massage, rub, pat, poke, tap, push, press, scratch, tickle	Imagination	Happy, excited, surprised, afraid, angry, disgusted, sad, depressed, tired, calm, relaxed, content	15	CNNs	92.41%	72.47%
Choi et al. <sup>14</sup>	Flexible transparent skin	Pressure, strain, position	Pat, tap, pinch, twist	×	×	×	×	×	×
Zhang et al. <sup>15</sup>	Soft epidermal electronics	Surface electromyography (sEMG)	×	Control expression	Surprise, fear, sadness, disgust, happiness, angry	1	CNNs	×	80.17%
Lee et al. <sup>17</sup>	Flexible facial interface	Strain, vibration	×	Control expression	Happiness, surprise, disgust, anger, sadness	1	CNNs	×	93.33%
This work	Flexible hairy interface	Pressure, position, stroke speed	Touch, pat, stroke, slap, push, tickle, press, knock	Video clips / SAM	Positive Neutral Negative	13	LSTM, CNN	99.00%	82.17%

DASS: Depression, Anxiety and Stress Scales; SAM: Self-Assessment Manikin; IADS: International Affective Digitized Sounds; HMM: Hidden Markov model; LSTM: Long short-term memory neural network; NN: Neural network; CNN:

Supplementary Table 6. State-of-the-art soft electronics for tactile mapping interface

Works	Interaction objects	If detect emotion	If consider contextual information	Decision making	Possible types of responses
Du et al. <sup>42</sup>	Robot car	Yes	No	Program presetting	6
Huang et al. <sup>43</sup>	Robot dog and virtual character	Yes	No	Program presetting	7
Choi et al. <sup>14</sup>	Virtual robot	Yes	No	Program presetting	4
Lee et al. <sup>17</sup>	Virtual character	Yes	Yes	Program presetting	N/A
This work	Robot dog	Yes	Yes	ChatGPT-based independent decision making	>820

## References:

- 1 Shapiro, D., Zhan, Z., Cottrell, P. & Isbister, K. Translating Affective Touch into Text. in *Extended Abstracts of the 2019 CHI Conference on Human Factors in Computing Systems* 1–6 (Association for Computing Machinery, Glasgow Scotland Uk, 2019).
- 2 Balducci, F., Impedovo, D., Macchiarulo, N. & Pirlo, G. Affective states recognition through touch dynamics. *Multimedia Tools and Applications* **79**, 35909–35926 (2020).
- 3 Wampfler, R., Klingler, S., Solenthaler, B., Schinazi, V. R. & Gross, M. Affective State Prediction Based on Semi-Supervised Learning from Smartphone Touch Data. in *Proceedings of the 2020 CHI Conference on Human Factors in Computing Systems* 1–13 (Association for Computing Machinery, New York, NY, USA, 2020).
- 4 Niu, S. *et al.* Theoretical investigation and structural optimization of single-electrode triboelectric nanogenerators. *Adv. Funct. Mater.* **24**, 3332-3340 (2014).
- 5 Qi, Y., Jia, W. & Gao, S. Emotion Recognition Based on Piezoelectric Keystroke Dynamics and Machine Learning. in *2021 IEEE International Conference on Flexible and Printable Sensors and Systems (FLEPS)*. 1-4 (IEEE, Manchester, United Kingdom, 2021).
- 6 Niewiadomski, R. & Sciutti, A. Multimodal Emotion Recognition of Hand-Object Interaction. in *26th International Conference on Intelligent User Interfaces* 351–355 (Association for Computing Machinery, New York, NY, USA, 2021).
- 7 Handler, A. & Ginty, D. D. The mechanosensory neurons of touch and their mechanisms of activation. *Nat. Rev. Neurosci.* **22**, 521-537 (2021).
- 8 Agramunt, J. *et al.* Mechanical stimulation of human hair follicle outer root sheath cultures activates adjacent sensory neurons. *Sci. Adv.* **9**, eadh3273 (2023).
- 9 Flagg, A. & MacLean, K. Affective touch gesture recognition for a furry zoomorphic machine. in *Proceedings of the 7th International Conference on Tangible, Embedded and Embodied Interaction* 25–32 (Association for Computing Machinery, Barcelona Spain, 2013).
- 10 Jung, M. M., Poppe, R., Poel, M. & Heylen, D. K. J. Touching the Void -- Introducing CoST: Corpus of Social Touch. in *Proceedings of the 16th International Conference on Multimodal Interaction* 120–127 (Association for Computing Machinery, New York, NY, USA, 2014).
- 11 Löken, L. S., Wessberg, J., Morrison, I., McGlone, F. & Olausson, H. Coding of pleasant touch by unmyelinated afferents in humans. *Nat. Neurosci.* **12**, 547-548 (2009).
- 12 Ku, H. J. *et al.* Online Social Touch Pattern Recognition with Multi-modal-sensing Modular Tactile Interface. in *2019 16th International Conference on Ubiquitous Robots (UR)* 271–277 (2019).

- 13 Li, Y.-K., Meng, Q.-H., Yang, T.-H., Wang, Y.-X. & Hou, H.-R. Touch Gesture and Emotion Recognition Using Decomposed Spatiotemporal Convolutions. *IEEE Trans. Instrum. Meas.* **71**, 1-9 (2022).
- 14 Choi, D.-S. *et al.* Emotion-interactive empathetic transparent skin cushion with tailored frequency-dependent hydrogel–plasticized nonionic polyvinyl chloride interconnections. *Chem. Eng. J.* **442**, 136142 (2022).
- 15 Zhuang, M. *et al.* Highly Robust and Wearable Facial Expression Recognition via Deep-Learning-Assisted, Soft Epidermal Electronics. *Research* **2021** (2021).
- 16 Vrontou, S., Wong, A. M., Rau, K. K., Koerber, H. R. & Anderson, D. J. Genetic identification of C fibres that detect massage-like stroking of hairy skin in vivo. *Nature* **493**, 669-673 (2013).
- 17 Lee, J. P. *et al.* Encoding of multi-modal emotional information via personalized skin-integrated wireless facial interface. *Nat. Commun.* **15**, 530 (2024).
- 18 Teysier, M., Bailly, G., Pelachaud, C. & Lecolinet, E. Conveying Emotions Through Device-Initiated Touch. *IEEE Trans. Affective Comput.* **13**, 1477-1488 (2022).
- 19 Hertenstein, M. J., Keltner, D., App, B., Bulleit, B. A. & Jaskolka, A. R. Touch communicates distinct emotions. *Emotion* **6**, 528-533 (2006).
- 20 McIntyre, S. *et al.* Affective touch communication in close adult relationships. in *2019 IEEE World Haptics Conference (WHC)* 175–180 (IEEE, Tokyo, Japan, 2019).
- 21 Bradley, M. M. & Lang, P. J. Measuring emotion: The self-assessment manikin and the semantic differential. *J. Behav. Ther. Exp. Psy.* **25**, 49-59 (1994).
- 22 Carneros-Prado, D. *et al.* Comparative Study of Large Language Models as Emotion and Sentiment Analysis Systems: A Case-Specific Analysis of GPT vs. IBM Watson. in *Proceedings of the 15th International Conference on Ubiquitous Computing & Ambient Intelligence (UCAmI 2023)* (eds Bravo, J. & Urzáiz, G.) 229–239 (Springer Nature Switzerland, Cham, 2023).
- 23 Krugmann, J. O. & Hartmann, J. Sentiment analysis in the age of generative AI. *Customer Needs and Solutions* **11**, 3 (2024).
- 24 Ren, J. T. Harnessing public sentiment: A literature review of sentiment analysis in energy research. *Renewable Sustainable Energy Rev.* **219**, 115739 (2025).
- 25 Eshraghian, J. K. *et al.* Training spiking neural networks using lessons from deep learning. *Proc. IEEE* **111**, 1016-1054 (2023).
- 26 Massari, L. *et al.* Functional mimicry of Ruffini receptors with fibre Bragg gratings and deep neural networks enables a bio-inspired large-area tactile-sensitive skin. *Nat. Mach. Intell.* **4**, 425-435 (2022).
- 27 Sun, H. & Martius, G. Guiding the design of superresolution tactile skins with taxel value isolines theory. *Sci. Rob.* **7**, eabm0608 (2022).
- 28 Park, K., Yuk, H., Yang, M., Cho, J., Lee, H. & Kim, J. A biomimetic

- elastomeric robot skin using electrical impedance and acoustic tomography for tactile sensing. *Sci. Rob.* **7**, eabm7187 (2022).
- 29 Lee, Y. *et al.* Triboresistive Touch Sensing: Grid-Free Touch-Point Recognition Based on Monolayered Ionic Power Generators. *Adv. Mater.* **34**, e2108586 (2022).
- 30 Shi, J. *et al.* Embedment of sensing elements for robust, highly sensitive, and cross-talk-free iontronic skins for robotics applications. *Sci. Adv.* **9**, eadf8831 (2023).
- 31 Xu, R. *et al.* Skin-Friendly and Wearable Iontronic Touch Panel for Virtual-Real Handwriting Interaction. *ACS Nano* **17**, 8293–8302 (2023).
- 32 Zhou, Y. *et al.* A multimodal magnetoelastic artificial skin for underwater haptic sensing. *Sci. Adv.* **10**, eadj8567 (2024).
- 33 Ye, C. *et al.* Sustainable Silk Fibroin Ionic Touch Screens for Flexible Biodegradable Electronics with Integrated AI and IoT Functionality. *Adv. Mater.* **37**, 2412972 (2024).
- 34 Kim, K. *et al.* Extremely durable electrical impedance tomography-based soft and ultrathin wearable e-skin for three-dimensional tactile interfaces. *Sci. Adv.* **10**, eadr1099 (2024).
- 35 Xia, Y. *et al.* Transparent Self-Healing Anti-Freezing Ionogel for Monolayered Triboelectric Nanogenerator and Electromagnetic Energy-Based Touch Panel. *Adv. Mater.* **36**, 2308424 (2024).
- 36 Kim, K. K., Ha, I., Won, P., Seo, D.-G., Cho, K.-J. & Ko, S. H. Transparent wearable three-dimensional touch by self-generated multiscale structure. *Nat. Commun.* **10**, 2582 (2019).
- 37 Oh, H., Yi, G.-C., Yip, M. & Dayeh, S. A. Scalable tactile sensor arrays on flexible substrates with high spatiotemporal resolution enabling slip and grip for closed-loop robotics. *Sci. Adv.* **6**, eabd7795 (2020).
- 38 Huang, Y.-C. *et al.* Sensitive pressure sensors based on conductive microstructured air-gap gates and two-dimensional semiconductor transistors. *Nat. Electron.* **3**, 59-69 (2020).
- 39 Zhong, D. *et al.* High-speed and large-scale intrinsically stretchable integrated circuits. *Nature* **627**, 313-320 (2024).
- 40 Cho, Y. *et al.* Three-Dimensional Touch Device with Two Terminals. *Adv. Mater.* **35**, 2305697 (2023).
- 41 Lee, Y. *et al.* Triboresistive Touch Sensing: Grid-Free Touch-Point Recognition Based on Monolayered Ionic Power Generators. *Adv. Mater.* **34**, 2108586 (2022).
- 42 Du, X. *et al.* An Ultra-Conductive and Patternable 40 nm-Thick Polymer Film for Reliable Emotion Recognition. *Adv. Mater.* **36**, e2403411 (2024).
- 43 Huang, J. *et al.* Deep Learning-Assisted Electronic Skin System Capable of Capturing Spatiotemporal and Mechanical Features of Social Touch to Enhance Human-Robot Emotion Recognition. *SmartMat* **6**, e1325 (2025).